Dust and Gas in NGC3627

Dust and Gas in NGC3627 Using Observations from SCUBA-2

By

Jonathan H. Newton, B.A.

A Thesis

Submitted to the School of Graduate Studies

in Partial Fulfilment of the Requirements

for the Degree

Master of Science

McMaster University

MASTER OF SCIENCE (2014)   McMaster University

(Physics and Astronomy)   Hamilton, Ontario

TITLE: Dust and Gas in NGC3627 Using Observations from SCUBA-2

AUTHOR: Jonathan Newton, B.A. (Western Kentucky University)

SUPERVISOR: Christine D. Wilson

NUMBER OF PAGES: viii, 70

Abstract

Saw some dust and wanted to do something about it!

To my family and Poly.

Acknowledgements

When life looks like easy street, there is danger at your door... -Robert Hunter

Thank Chris and group members of course. Don't forget Christian!

Table of Contents

List of Figures

List of Tables

Chapter 1

Introduction

1.1 The Physical Processes of Star Formation

Star formation is one of the fundamental processes in astrophysics that affects not just stellar and planetary formation but also dictates the behavior in galaxy formation and evolution (Kennicutt & Evans, 2012). The study of star formation itself can be broken into several areas such as: the processes that trigger collapse and how the collapse behaves, dictating how and what type of stars can form from a given region or cloud, or how the inflow of new material can alter current star forming environments. These different sub-branches of star formation are conveniently sorted into hierarchal schemes that range from Mpc scales seen in gas accretion from the intergalactic medium, to properties of accretion disks on scales of the order $R_\odot$ or AU(Kennicutt & Evans, 2012). In this body of work we focus on the physical properties of the dust and abundance of gas in the giant molecular cloud (GMC) phase of star formation prior to stellar collapse or fragmentation. However based on the resolution of

our target galaxy, we will not be able to examine individual GMCs instead we will need to focus our work on giant molecular associations (GMAs).

1.1.1 GMC Formation

After the intergalactic gas has accreted into a host galaxy, it will eventually condense and begin to form a GMC (Kennicutt & Evans, 2012). The condensation of this gas leads to the formation of molecular clouds. The dominant process of GMC formation is divided between two camps; either a "bottom-up" or "top-down" formation scenario (McKee & Ostriker, 2007). The bottom-up scenario consists of small clouds of cold HI coagulating to eventually form a GMC (Field & Saslaw, 1965; Kwan, 1979). The major concern with the bottom-up scenario is if we include heating mechanisms in the cloud, coagulation will cease before the observed masses are reached (McKee & Ostriker, 2007). In fact, the time scales required to form a cloud typical of what we observe would take around 10^8 years to accumulate a minimum of 10^5 M$_\odot$, which is much greater than the expected GMC lifetime (McKee & Ostriker, 2007).

The alternative formation scenario, top-down, postulates the GMC formation comes from instabilities in the diffuse ISM causing the clouds to collapse from their surrounding medium (McKee & Ostriker, 2007). Two main instabilities are thought to be responsible for the collapse. The first type of instability is a Parker instability, which involves distortion of magnetic fields lines in the mid plane of the galaxy, and at these distortions gas will begin to accumulate (Parker, 1966; Dobbs et al., 2013). The second instability re-

sponsible for collapse comes in the style of a more complex Jeans instability which is determined further by the amount of rotational shear present (McKee & Ostriker, 2007). If a strong rotational shear is present, such as in the inter arm region of a spiral galaxy, then a process known as swing amplification will occur (McKee & Ostriker, 2007). If no rotational shear is present, such as the inner regions of a galaxy or spiral arms, then the collapse can be attributed to a magneto-Jeans instability (Elmegreen, 1987; Kim & Ostriker, 2001).

1.1.2 Molecular Hydrogen Formation

Regardless of either collapse or coagulation, molecular hydrogen is being formed inside the cloud. The formation of molecular hydrogen can be summarized using either the two body reaction, three body reaction, formation using a free electron or proton, or surface formation (Krumholz, 2014). The two body formation scenario is the simplest reaction using two hydrogen atoms to produce molecular hydrogen, reaction 1.1.

$$H + H \longrightarrow H_2 \tag{1.1}$$

However the two body formation is not the major mechanism in the formation of H_2 due to the requirement of a forbidden photon that arises from the combination of hydrogen atoms in the ground state (Gould & Salpeter, 1963). If one of the hydrogen atoms is excited, the transition can occur and molecular hydrogen is formed, but the amount of excited hydrogen atoms in

the temperature ranges typical of the cold and warm phases of the ISM are expected to be nearly nonexistent (Krumholz, 2014).

The second formation scenario listed, the three body formation, involves three hydrogen atoms coming together to form molecular hydrogen with a spare hydrogen atom shown in reaction 1.2.

$$3\,\mathrm{H} \longrightarrow \mathrm{H}_2 + \mathrm{H} \tag{1.2}$$

The required density for the three body formation to occur is on the order of $10^8\ \mathrm{cm}^{-3}$ (Palla et al., 1983; Abel et al., 1997), while the typical GMC density is on the order of $300\ \mathrm{cm}^{-3}$. The disparity between these densities eliminates any possibility of this being the primary mechanism to form molecular hydrogen.

An alternative to the two or three body reactions uses either an electron or proton to ionize the hydrogen forming either H^- or H_2^+ (Krumholz, 2014). The chemical reaction involving an electron is shown in reaction 1.3 and reaction utilizing a proton is shown in reaction 1.4

$$\mathrm{H} + e \longrightarrow \mathrm{H}^- + h\nu$$
$$\mathrm{H}^- + e \longrightarrow \mathrm{H}_2 + e \tag{1.3}$$

$$\mathrm{H} + \mathrm{H}^+ \longrightarrow \mathrm{H}_2^+ + h\nu$$
$$\mathrm{H}_2^+ + \mathrm{H} \longrightarrow \mathrm{H}_2 + \mathrm{H}^+ \tag{1.4}$$
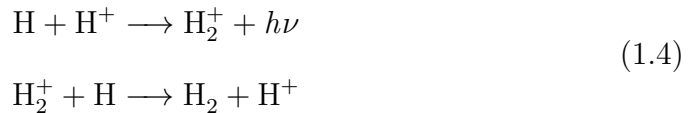
The main limitation of the free electron/proton formation mechanism is an undersupply of free electrons and protons. Typical Milky Way conditions show that regions $>1\ \mathrm{cm}^{-3}$ have free electron and proton densities $<10^{-4}\ \mathrm{cm}^{-3}$

(Wolfire et al., 2003). Secondly, the H^- ion in reaction 1.3 is more likely to interact with a stray photon than an electron resulting in the ion returning to the atomic state (Glover, 2003). While we observe singly ionized hydrogen regions, HII regions, only a small fraction of the region will successfully produce molecular hydrogen.

While the free electron/proton formation method is suspected to be the primary H_2 catalyst in the early universe (Herbst et al., 2005), at low redshifts the formation of molecular hydrogen on the surface of dust grains is the dominant mechanism of formation (Krumholz, 2014). The surface formation of molecular hydrogen will occur when a hydrogen atom strikes a dust grain and successfully sticks to the grain. The hydrogen then will then interact with another hydrogen atom to form H_2 and be ejected from the dust particle after the reaction has occurred (Pirronello et al., 1997). The same process occurs on the dust grain as the two body formation, but the dust grain will act as a medium to absorb the energy that would create the forbidden photon (Krumholz, 2014).

With a dominant mechanism for molecular hydrogen formation, a reaction rate can be defined based on the cross section of the grain, Σ_{gr}, a striking probability dependent on the temperature of the observed dust, S(T), the probability of molecular hydrogen forming on the grain, ϵ_{H_2}, the density of free hydrogen in the GMC, n_H, and the density of hydrogen attached to the grain surface, n_{H0} (Krumholz, 2014). Scaling this with the integrated collisional probability of a Maxwellian gas, a reaction rate is determined to be equation

1.5 where k_b is the Boltzmann constant, T is the temperature, and m_H is the mass of the hydrogen atom.

$$\frac{dn_{H_2}}{dt} = \frac{1}{2} \left(\frac{8k_bT}{\pi m_H} \right)^{\frac{1}{2}} \Sigma_{gr} S\left(T\right) \epsilon_{H_2} n_H n_{H_0} \tag{1.5}$$

Equation 1.5 is often simplified to equation 1.6 by introducing a variable known as the formation rate, $\mathcal{R}_{gr}$, that is constrained using the column densities CI, CII, HI, H_2. Typical reaction rates for the Milky Way have been found to be $3x10^{-17}cm^3s^{-1}$ (Jura, 1975; Gry et al., 2002; Wolfire et al., 2008).

$$\frac{dn_{H_2}}{dt} = \mathcal{R}_{gr} n_H n_{H_0} \tag{1.6}$$

1.1.3 Dissociation of Molecular Hydrogen

When the molecular hydrogen has formed, it is still susceptible to photodissociation from far ultra-violet (FUV) photons. The energy required for a single photon to break the bonds of molecular hydrogen is 14.5 eV (Krumholz, 2014). Conveniently, this is also enough energy to excite atomic hydrogen, so photodissasociation using a single photon is highly unlikely due to the abundance of HI in the ISM (Krumholz, 2014). However, a photon with an energy of 11-13.6 eV will not be able to excite atomic hydrogen, but will be able to excite the molecular hydrogen to its first and second excitation levels, the Lyman and Werner bands respectively. The excited H_2 will eventually settle via photon emission to its ground state with a finite probability of returning

to two hydrogen atoms rather than maintaing its molecular state (Krumholz, 2014).

A dissociation rate, ζ_{diss}, can be obtained by scaling the total excitation rate, ζ_{exc}, by the fraction of excited hydrogen molecules that will settle to an atomic ground state (Krumholz, 2014). The total excitation rate is found by summing each of individual excitations from the ground state e.g. $\zeta_{exc,0-1}$, $\zeta_{exc,0-2}$. In the Milky Way's diffuse ISM, the interstellar radiation field is 6-9x10^{-14} erg cm^{-3} over the range of 6-13.6 eV resulting in $\zeta_{exc} \approx 3 \times 10^{-10}$s^{-1} (Draine, 2011). The expected fraction of H$_2$ to disassociate is between 0.11 and 0.13 resulting in $\zeta_{diss} \approx 4 \times 10^{-11}$s^{-1}(Draine, 2011). Equating the formation and dissociation rates and then solving for a molecular hydrogen vs atomic hydrogen ratio gives in equation 1.7 (Krumholz, 2014). From equation 1.7 we can see, in the diffuse medium, atomic hydrogen is far more abundant than molecular hydrogen, as expected.

$$
\begin{aligned}
\zeta_{diss} n_{H_2} &= \mathcal{R} n_{H_0} n_H \\
\frac{n_{H_2}}{n_H} &= \frac{\mathcal{R} n_{H_0}}{\zeta_{diss}} \\
&= 8 \times 10^{-6} \left(\frac{4 \times 10^{-11} s^{-1}}{\zeta_{diss}} \right) \left(\frac{n_{H_0}}{10 cm^{-3}} \right)
\end{aligned}
\tag{1.7}
$$

However, as the density of the gas increases via collapse or coagulation, the optical depth will also increase limiting the amount of FUV photons able to penetrate into the core of the cloud, a process known as shielding (Draine, 2011). This shielding will aid in the decrease of ζ_{diss} which will increase the value in equation 1.7. The increase in molecular to atomic hydrogen ratio signifies the accumulation of molecular gas reservoirs. The molecular gas build

up will lead to fragmentation within the cloud, and will eventually lead to forming stars.

1.2 Determining H_2 Abundance

From the previous section, the formation of molecular hydrogen will result in the energy released during creation to be absorbed by a dust grain rather than through emission resulting in H_2 creation being a dark process, §1.1.2. Furthermore, since the molecule is made of two hydrogen atoms, the high symmetry and low mass will negate any permanent dipole effects (Bolatto et al., 2013; Kennicutt & Evans, 2012). This does not mean the H_2 is unexcitable, but the temperatures required to excite molecular hydrogen are (T $\gtrsim$ 100K) above the temperature of a typical GMC(Bolatto et al., 2013), and the settling of H_2 will more often than not result in the molecule separating into two hydrogen atoms §1.1.3. For our purposes, we can consider molecular hydrogen a dark molecule requiring special treatment to determine the amount present.

Calculating the amount of molecular hydrogen in a system can be performed in several ways, and for the purpose of extragalactic sources they all involve using the amount of a molecular tracer to determine how much H_2 is present. Molecules such as OH have been used in the past however mainly for Milky Way targets (Barrett, 1964). The molecule most commonly used in extragalactic studies is CO due to it's plentiful amount and ability to be easily observed (Bolatto et al., 2013). The amount of CO determined can then be converted to H_2 using a conversion factor (either X_{CO} or α_{CO} depending on whether the final solution is in terms of column density or surface density).

1.2.1 Methods for Determining CO-to-H_2 Conversion Factor

Several methods are present to determine the conversion factor each with their own caveats. One common method used to determine a conversion factor is to utilize the virial nature of GMCs (Bolatto et al., 2013). This method works best for well defined clouds, however in the case of more distant nearby galaxies, the issue of whether or not the GMAs will display the same virialization as their constituent GMCs can hinder the results (Bolatto et al., 2013). The second caveat of using the virial mass to determine a conversion factor is the method will only trace CO bright regions which lead to opposing results with other methods (Bolatto et al., 2013). The mechanism behind this discrepancy is believed to be due to weak dust shielding that corresponds to a low metallicity. The low metalicity will allow the CO to be dissociated resulting in large amounts of molecular hydrogen traced by ionized and atomic carbon gas instead of CO. (Bolatto et al., 2013).

A second method to ascertain a conversion factor is to incorporate observations of isotopologues of CO that are optically thin, commonly ^{13}CO (Bolatto et al., 2013). The temperature, density, and column or surface density of the ^{13}CO can be used to restrict the possible outcomes of the physical conditions of the GMC or GMA being examined. In addition to degeneracies in the radiative transfer models, this method shares the same problem as the virial technique in that it only probes CO bright regions of the target leaving any CO-faint H_2 gas untraced (Bolatto et al., 2013). The issue of CO-faint gas has been examined using the photodissociated tracer of CO, [CII], in dwarf galaxies to reveal large reservoirs of self-shielding H_2 (**?**).

The third major way to determine a CO-to-H_2 conversion factor is by incorporating the emission from dust to determine the amount of molecular gas present. This assumes that the gas is well mixed with a constant ratio of dust and gas present in the galaxy (**?**), which has been shown to be true for the Milky Way (**?**). A suitable conversion factor is found by solving equation 1.8.

$$\delta_{GDR}\Sigma_{dust} = \Sigma_{H_2} + \Sigma_{HI}$$
$$= \alpha_{CO}I_{CO} + \Sigma HI \tag{1.8}$$

Where Σ_{dust}, Σ_{H_2}, and Σ_{HI} are the respective surface densities, I_{CO} is the CO line intensity, α_{CO} is the conversion factor in $M_\odot$ pc^{-2} K^{-1} km^{-1} s, and δ_{GDR} is the total mass of the gas divided by the total mass of the dust known as the dust-to-gas ratio (**?**Sandstrom et al., 2013). In equation 1.8, we can measure Σ_{dust}, Σ_{HI}, and I_{CO} leaving only the conversion factor and dust-to-gas ratio free to vary. An appropriate α_{CO} value will generate a molecular gas mass that produces a constant dust-to gas-ratio over the galaxy being studied, and has been carried out extensively by Sandstrom et al. (2013) on kpc^2 scales on nearby galaxies as well as on both of the Magellenic clouds (**?**).

Determining a conversion factor in this manner, allows the capability to trace the CO faint regions of target unlike the previous methods (**?**). Despite this advantage over the other two methods, using equation 1.8 leaves any gas not associated with atomic hydrogen to be left as H_2 increasing the conversion factor and overall amount of molecular hydrogen (Bolatto et al., 2013). Another caution of this method rests with the assumption of a constant

dust-to-gas ratio (Bolatto et al., 2013). Issues such as the dependence with metallicity (**?**) can render this assumption null if not treated properly. Nevertheless, given the agreement of conversion factors between this method and other methods used, suggests that any added bit of gas, incorrectly assumed to be H_2, and local fluctuations in metallicity of the target galaxy have very little effect on the final results, (Bolatto et al., 2013).

Chapter 2

Observations and Data Preparation

2.1 SCUBA-2

The Submillimetre Common-User Bolometer Array 2 (SCUBA-2) was designed to decrease the observing time of the sub-millimeter sky relative to its predecessor SCUBA (Holland et al., 2013). This would benefit the community by allowing for rapid data acquisition in the submillimeter regime of the electromagnetic spectrum, at the 450μm and 850μm bands in particular. Prior to SCUBA-2, other bolometer cameras such as LABOCA, BOLOCAM and SHARC-II were limited to less than 100 pixels, while the new SCUBA-2 has been able to incorporate over 10,000 pixels in its design and effectively reduce the required observing time (Chapin et al., 2013). Increasing the amount of pixels by a factor of 100 was possible by the advent of new technology such as high precision micromachining, superconducting transition edge sensors, and superconducting quantum interference device amplifiers (SQUIDs) (Holland et al., 2013).

The observations of NGC3627 were taken from the Nearby Galaxies Legacy Survey's (NGLS) initial science images using SCUBA-2 from December 29, 2011 to January 21, 2012, and consist of 24 18′ by 18′ scans taken in grade 3 weather or better ($0.08 < \tau < 0.12$) with observations centered at 450μm and 850μm emission with a 32μm and 85μm bandpass respectively. 16 of the 24 scans were deemed useable, and whether or not an observation was deemed worthwhile was determined by factors such as the behavior of the image background or whether the image was flagged during observing to be unusable. The observations of NGC3627 were taken using a daisy scanning pattern to help remove any random noise by introducing crossing points. The scanning speed of the JCMT was 150″/second in order to negate any drifting effects seen from the instrument or sky (Chapin et al., 2013).

2.2 Image Creation and Properties

For any imaging process to be successful, the final image needs to have a limited white noise (Chapin et al., 2013). White noise in the sense of our bolometer observations arises from thermal variations in the instrument and atmosphere during data acquisition. The random noise is minimized through scanning methods and during image processing (Chapin et al., 2013). To create the final SCUBA-2 data products, we use the Submillimetre User Reduction Facility (SMURF) procedure MAKEMAP. This procedure reduces the noise of the observations while maintaining the source's emission by incorporating a combination of principal component analysis and a maximum likelihood analysis (Chapin et al., 2013). Both of these methods have proven useful in

13

reducing bolometer data on their own, but due to the size of raw SCUBA-2 data, either method on its own would result in extreme run times or the process becoming resource intensive (Chapin et al., 2013).

MAKEMAP breaks down the image creation into several steps performed in iteration in order to successfully reduce any background noise (Chapin et al., 2013). The raw data is approximated by equation 2.1 such that $b_i(t)$ is the ith bolometer output at time t, f is a scaling factor determined from flat field calibrations, $e_i(t)$ is the extinction at time t for the ith bolometer, $a_i(t)$ is the astronomical signal for i^{th} bolometer at time t, $g_i * n_c(t)$ is the noise due to the product of the common mode and gain, $n_f(t)$ is the low-frequency noise, and $n_r(t)$ is the random noise (Chapin et al., 2013).

$$b_i(t) = f\left[e_i(t) * a_i(t) + g_i * n_c(t) + n_f(t) + n_r(t)\right] \qquad (2.1)$$

The steps used in MAKEMAP are designed so they can estimate each noise component of the bolometer signal. The COM and GAI steps estimate a common mode signal by fitting the average time-series of each bolometer observation. The next step is EXT, which is used to apply the measured extinction corrections. Following EXT is FLT to apply high- and low-pass filters to remove any noise features not removed in the COM and GAI filtering. After the high- and low-pass filters, the AST step is performed. AST converts the data from a time series to an image and detects sources to be removed from reduction. The sources removed during this portion of MAKEMAP are intended to be astronomical in nature. The final step is NOI which determines the noise in the gridded map after each step has been performed and is calcu-

14

lated by isolating the white noise component in equation 2.1. A convergence check is then issued based on the magnitude of change in each pixel from the previous map and the current version. If the check fails, the COM, GAI, EXT, and FLT values are recalculated using the AST information obtained from the previous iteration, and the process is repeated until the convergence values are met or the maximum number of iterations have been carried out (Chapin et al., 2013).

In our production of maps, we used the configuration file dimmconfig_bright_compact.lis and altered the AST and FLT sections of the image creation by introducing a mask made from Herschel's 250μm map. The purpose of the mask was to exclude the target from interfering with the noise minimization as well as prohibit any emission from the galaxy to be significantly altered during image production. The filter size of the high-pass filter was also modified, and an appropriate value was determined to be $175''$. We determined an appropriate high-pass filter size by running a large range of filters from $100''$ to $300''$ and inspecting the total recovered flux of NGC3627. A plot of the returned flux values can be seen in figure 2.1. An good filter would not show any significant decrease in flux compared to the 350μm or 500μm. This requirement removes any filters greater than $200''$. Given the flux was nearly constant with filters less than $200''$, we chose an appropriate filter size by examining the structure that was returned, in particular how well the spiral arms were recovered for the 850μm, and how well the disk was preserved in the 450μm. The spatial effect of the filters can be seen in figure 2.2 for the 450μm and figure 2.3 for the 850μm. The maps were returned from MAKEMAP in units of pW with a pixel size of $2''$ by $2''$ for both the 450μm and 850μm.
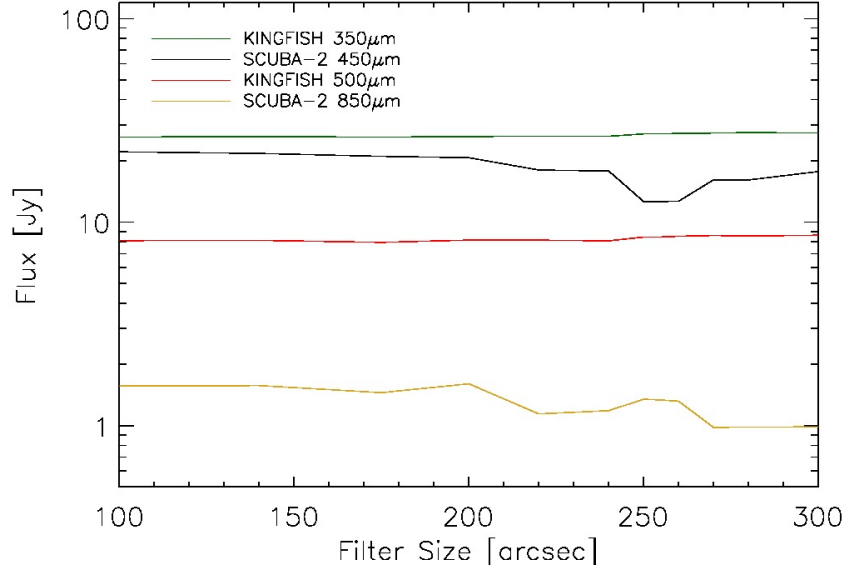
15

Figure 2.1: Returned flux values for NGC3627 with varying high-pass filter sizes. The KINGFISH fluxes have been been processed using the fakesource process, §2.4.2

The finalized $450\mu m$ image was then re-gridded down to a $4''$ by $4''$ pixel grid, and flux calibration values of 491000 and 4710 were applied to convert from pW to mJy/beam and mJy/square arcsecond, respectively. The $850\mu m$ maps were re-gridded to an $8''$ by $8''$ pixel size and used flux calibration values of 537000 and 2340 for mJy/beam and mJy/square arcsecond. The $4''$ and $8''$ pixels corresponded to a 180pc and 360pc size scale for our target, NGC3627. To simplify the analysis, the images are also converted to Jy/pixel. The $450\mu m$ and $850\mu m$ images are shown in figures 2.4 and 2.5. The calibration values used are the default flux calibration factors that are determined from our calibrator source, Uranus. The overall noise in the final image can be seen in table 2.1.
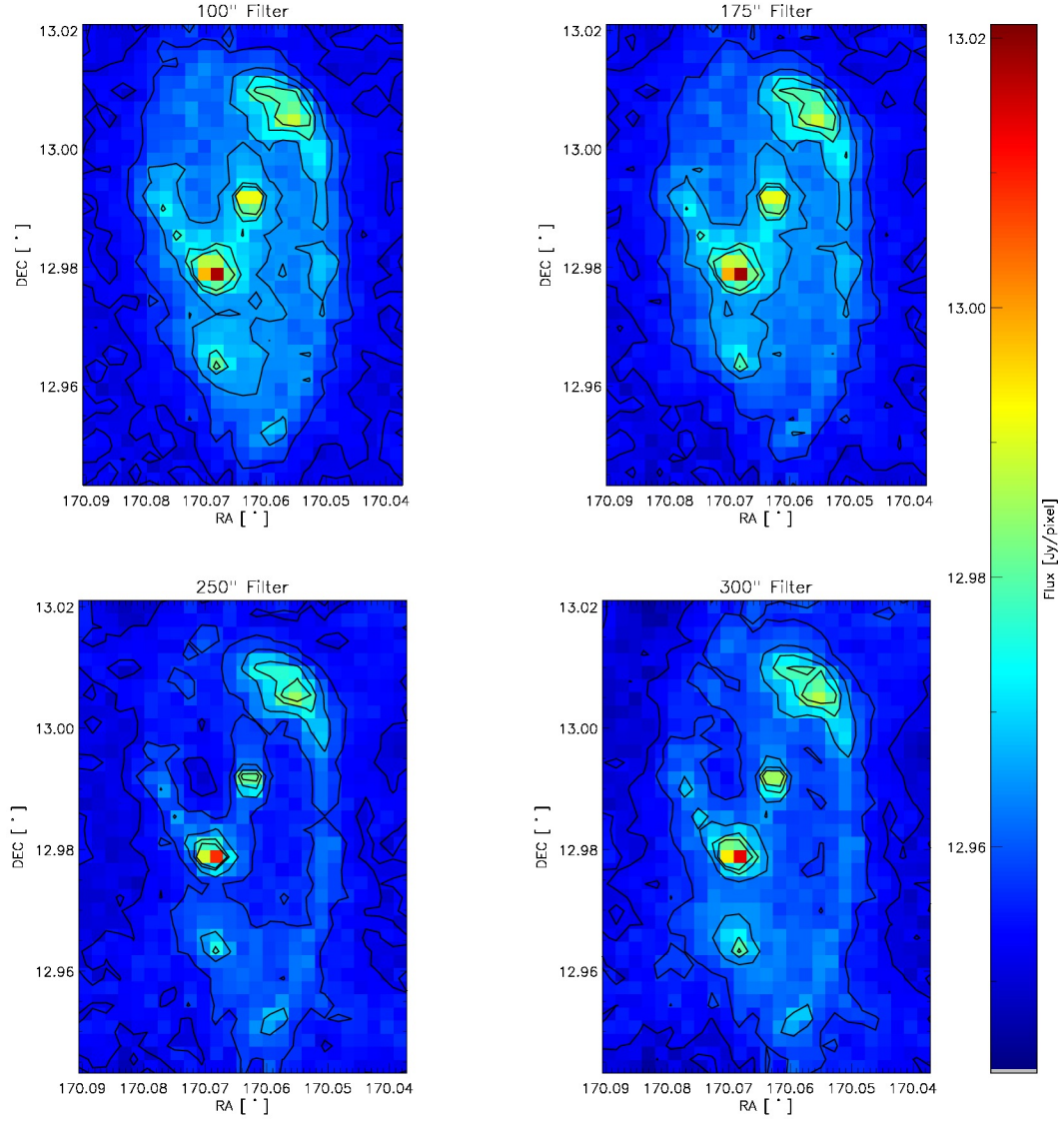
Figure 2.2: Four 450μm maps of NGC3627 using varying high-pass filter sizes. The contours shown are for 0.0, 0.02, 0.05, 0.08 and 0.1 Jy/pixel for each image.
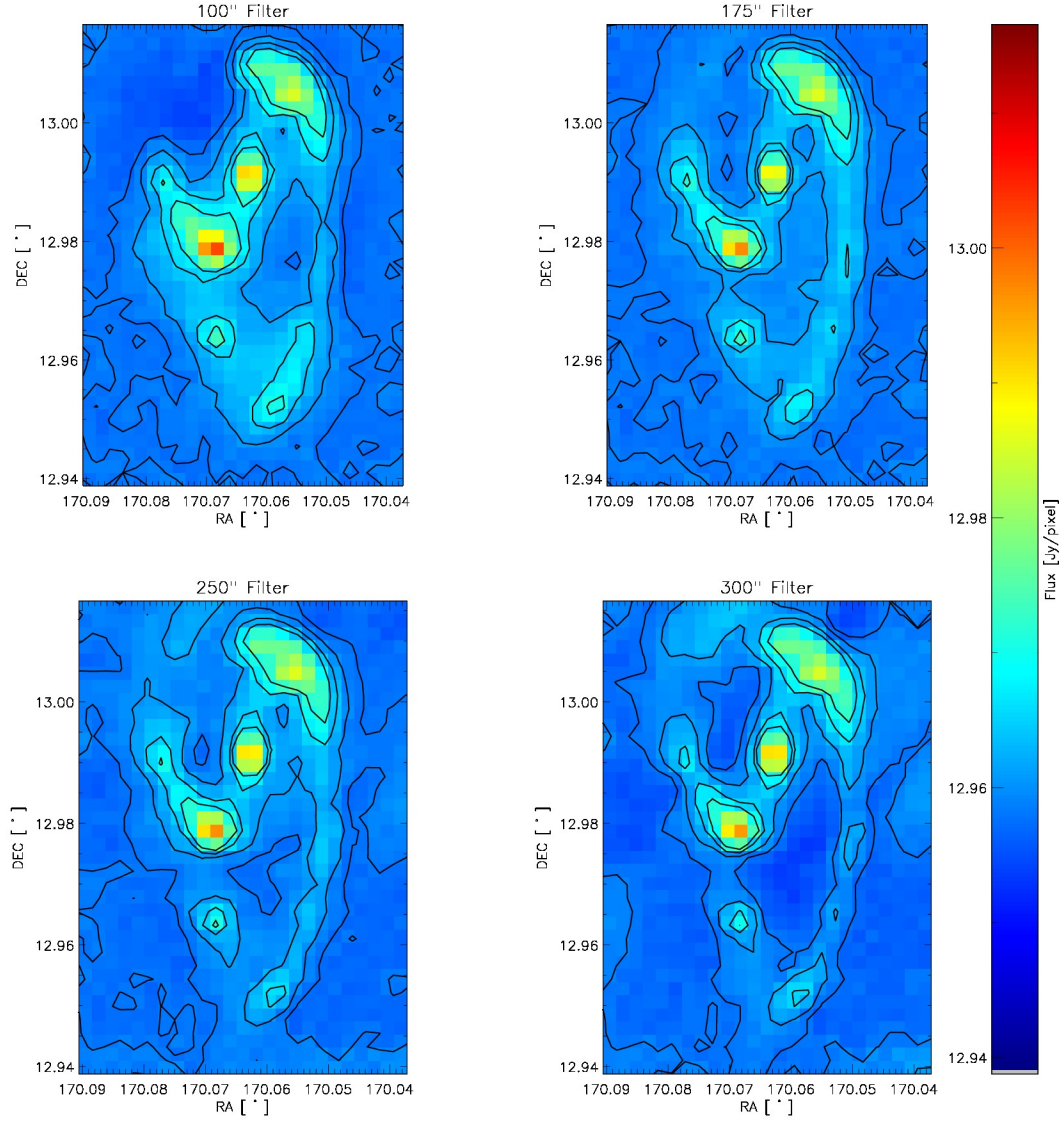
Figure 2.3: Four 850μm maps of NGC3627 using varying high-pass filter sizes. The contours shown are for 0.0, 0.002, 0.005, and 0.008 Jy/pixel for each image.
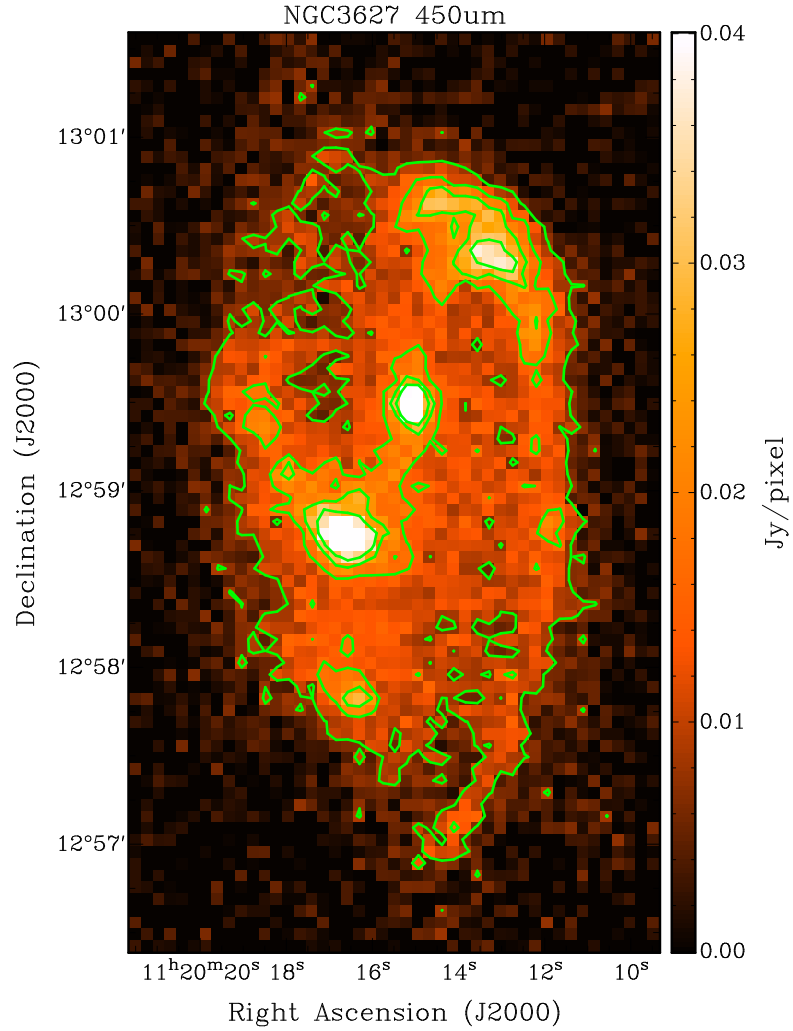
Figure 2.4: 450μm observation produced at the end of the image production with 20%, 40%, 60%, and 80% contours.

Table 2.1. Properties of NGC3627 SCUBA-2 Observations

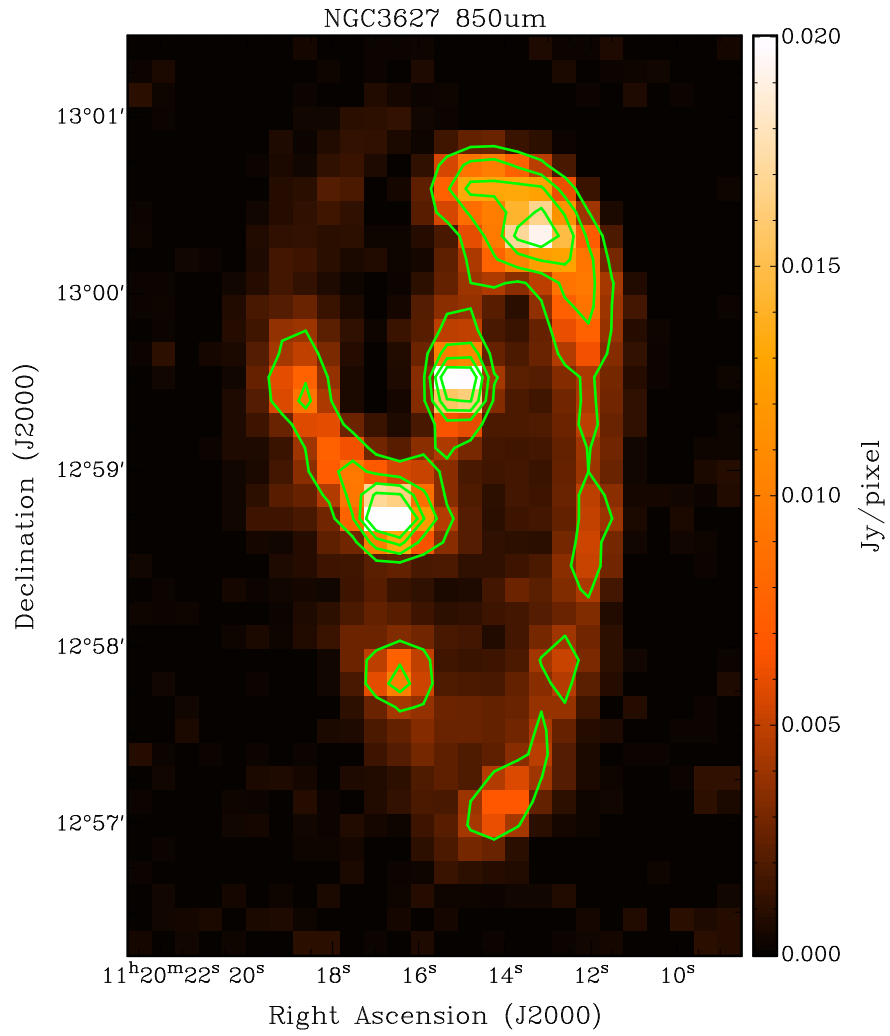| Observation	Beam Properties				RMS
	α	θ_α	β	θ_β	$[mJy\ /\ Pixel]$
450μm	0.854 ± 0.002	$7.48'' \pm 0.03''$	0.146 ± 0.003	$23.1'' \pm 0.2''$	3.42
850μm	0.9624 ± 0.0002	$12.8'' \pm 0.004''$	0.0376 ± 0.0002	$44.5'' \pm 0.09''$	0.476

19

Figure 2.5: 850μm observation produced at the end of the image production with 20%, 40%, 60%, and 80% contours.

2.2.1 Beam Shape of the 450μm and 850μm Data

The Uranus calibration images were used to determine the shape of the beam for the 450μm and 850μm observations. The beam shape of both the 450μm and 850μm maps deviates from a single gaussian due to the second maximum of the airy diffraction pattern in the response function of the telescope and minor imperfections in the mirror of the JCMT due to boundaries of the panels (Dempsey et al., 2013). This abnormality is best represented by a sum of two gaussians whose amplitude totals to unity (Dempsey et al., 2013). The average beam resolution for the 450μm and 850μm are reported in table 2.1 and match the values within uncertainty found in Dempsey et al. (2013). The calibration images, fitted beams, and the residual of the fits can be seen in figure 2.6. The contribution of the error beam in the 850μm emission is negligible, and allows the beam to be approximated by a single gaussian. However, the contribution of the error beam in the 450μm images was large enough to require special treatment in order to properly match the beams for analysis.

2.3 Ancillary Data

The scientific goals of this thesis required data outside the capabilities of SCUBA-2. For instance, accurately determining the dust mass involved fitting the spectral energy distribution (SED) for NGC3627. To successfully fit an SED, we needed shorter wavelength data to fully probe the cold component of this galaxy. We used data ranging from 100μm to 500μm from the KINGFISH survey (Kennicutt et al., 2011) to gain a large enough wavelength range for fitting the cold component. Secondly, the bandpass of the 850μm emission

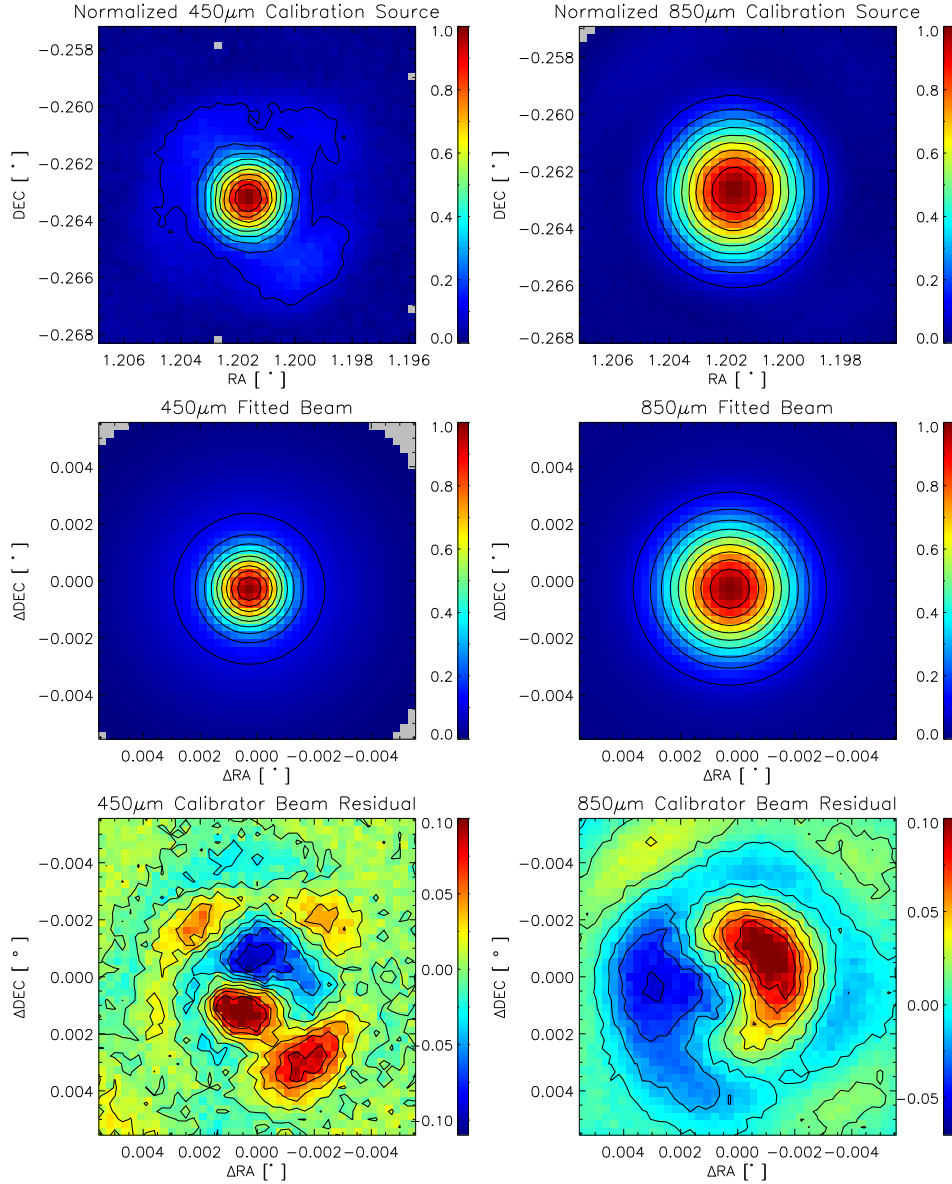Figure 2.6: The top row shows the Uranus images taken on January, 8th 2012 for the 450μm on the left and the 850μm on the right. The middle row shows the fitted beams for the 450μm on the right and 850μm on the left using the double gaussian beam shape. The bottom row shows the difference between the original image and the fitted beam. The contours in the image are from 10% to 90% in intervals of 10%.

contains the CO J=3-2 transmission line. In order to get a valid measurement of the dust mass, this contribution had to be removed. We used emission data from the NGLS using the HARP instrument on the JCMT (Wilson et al., 2012) to fulfill this role. When a dust mass was obtained, we used CO J=1-0 from the Nobeyama 45-m telescope (Kuno et al., 2007), CO J=2-1 from HERACLES (Leroy et al., 2009), and HI observations from THINGS (Walter et al., 2008) to determine a reasonable molecular hydrogen mass to calculate a dust-to-gas ratio.

2.3.1 Key Insights on Nearby Galaxies: a Far-Infrared Survey with Herschel (KINGFISH)

The Key Insights on Nearby Galaxies: a Far-Infrared Survey with Herschel (KINGSFISH) was designed to be a follow up to the Spitzer Infrared Nearby Galaxies Survey (SINGS) (Kennicutt et al., 2003) with observations of the warm and cold component of dust emission using the increased resolution from Herschel (Kennicutt et al., 2011). The main science goals of the KINGFISH survey were to better understand the star formation processes that were shielded by dust, resolved studies of heating and cooling of the interstellar medium (ISM), and to build an inventory of how cold dust emission relates to other dust components in the ISM (Kennicutt et al., 2011). The survey consisted of studying 61 nearby galaxies (d<30Mpc) that cover a range of environments. Each target was observed at 70μm, 100μm, 160μm, 250μm, 350μm, and 500μm. Our analyis focuses on fitting the cold component of NGC3627's SED, so we omitted the 70μm emission from the fitting, and pro-

Table 2.2.   Properties of NGC3627 KINGFISH Observations

Observation	Beam Properties θ_{beam}	RMS [mJy/Pixel]	Percentage of Emission Removed
100μm	6.8″	2.24	11%
160μm	11.6″	3.95	17%
250μm	18.0″	2.47	20%
350μm	24.9″	1.08	21%
500μm	36.0″	0.387	28%

cessed the data through MAKEMAP as described in § 2.4. The rms and beam size after the large scale structure has been removed can be seen in table 2.2, while the preconvolved maps are shown in figures 2.7 to 2.11.

2.3.2 Nearby Galaxies Legacy Survey (NGLS)

The Nearby Galaxies Legacy Survey is an HI-selected set of 155 galaxies contained in the annulus of $2Mpc \leq r \leq 25Mpc$ observed using the instrumentation on the JCMT (Wilson et al., 2012). The NGLS consists of data observed in several wavelengths that include the 450μm and 850μm data used for this thesis. As mentioned previously, the bandpass for SCUBA-2's 850μm emission contains the CO J=3-2 line which is contained in the NGLS data set. We used the zeroth moment CO J=3-2 maps from the NGLS to determine the percentage of CO J=3-2 emission present in the 850μm band as well as removing it for an accurate SED analysis. The rms and resolution of the CO J=3-2 emission are shown in table 2.3, and the scan prior to convolution is shown in figure 2.12.
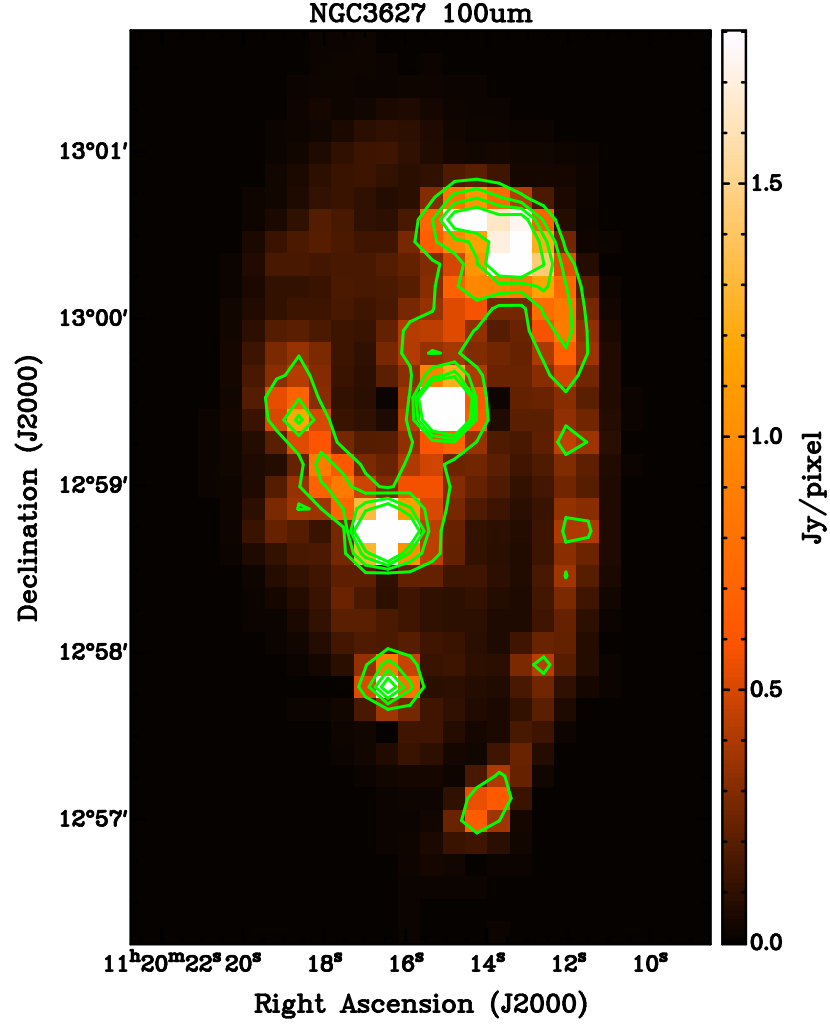
Figure 2.7: Image after the MAKEMAP filtering of 100μm observations with 20%, 40%, 60%, and 80% contours.

Table 2.3. Properties of NGC3627 NGLS Observations

Observation	Beam Properties θ_{beam}	RMS $[mJy/Pixel]$	Percentage of Emission Removed
CO J=3-2	14.5″	1.28e-2	29.8%

Figure 2.8: Image after the MAKEMAP filtering of 160μm observations with 20%, 40%, 60%, and 80% contours.
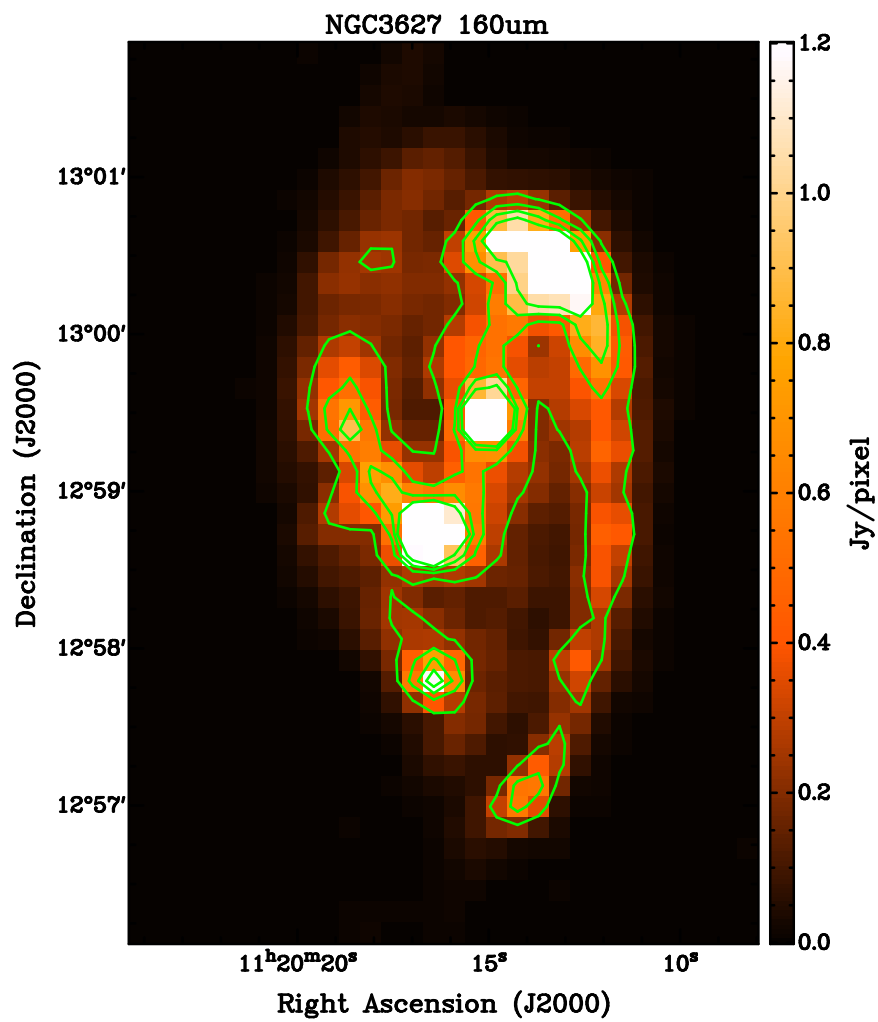
Figure 2.9: Image after the MAKEMAP filtering of 250μm observations with 20%, 40%, 60%, and 80% contours.

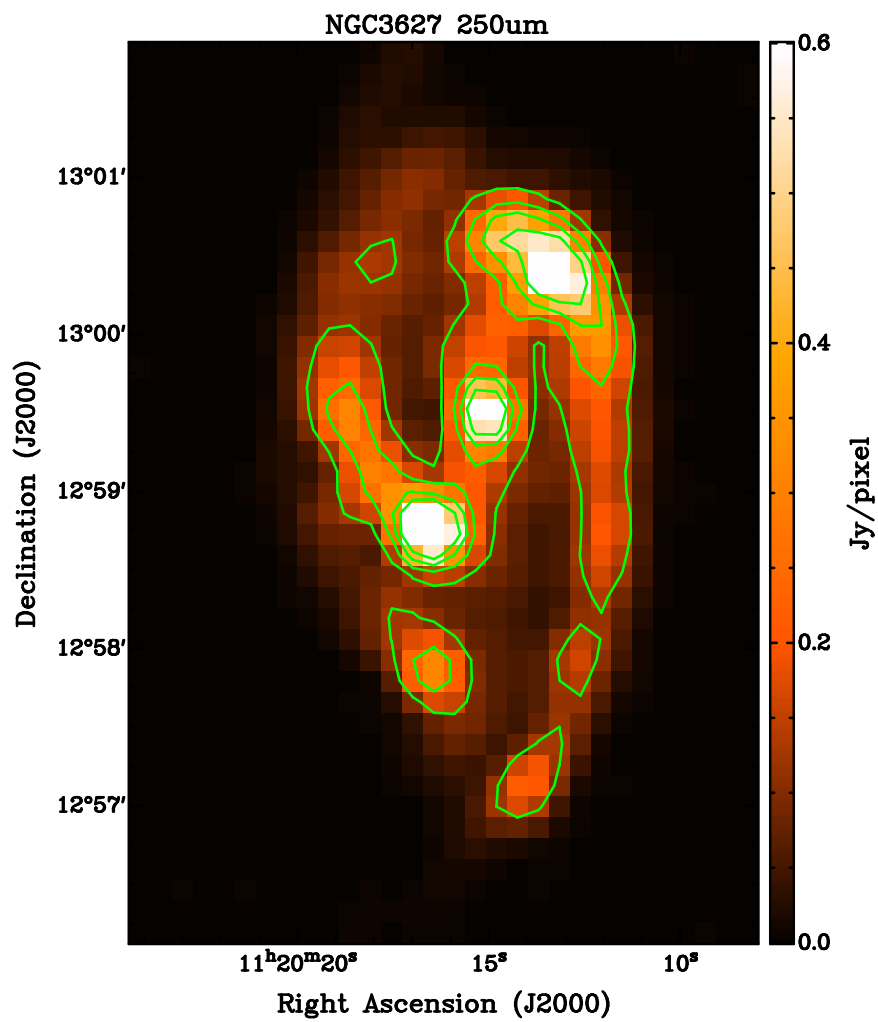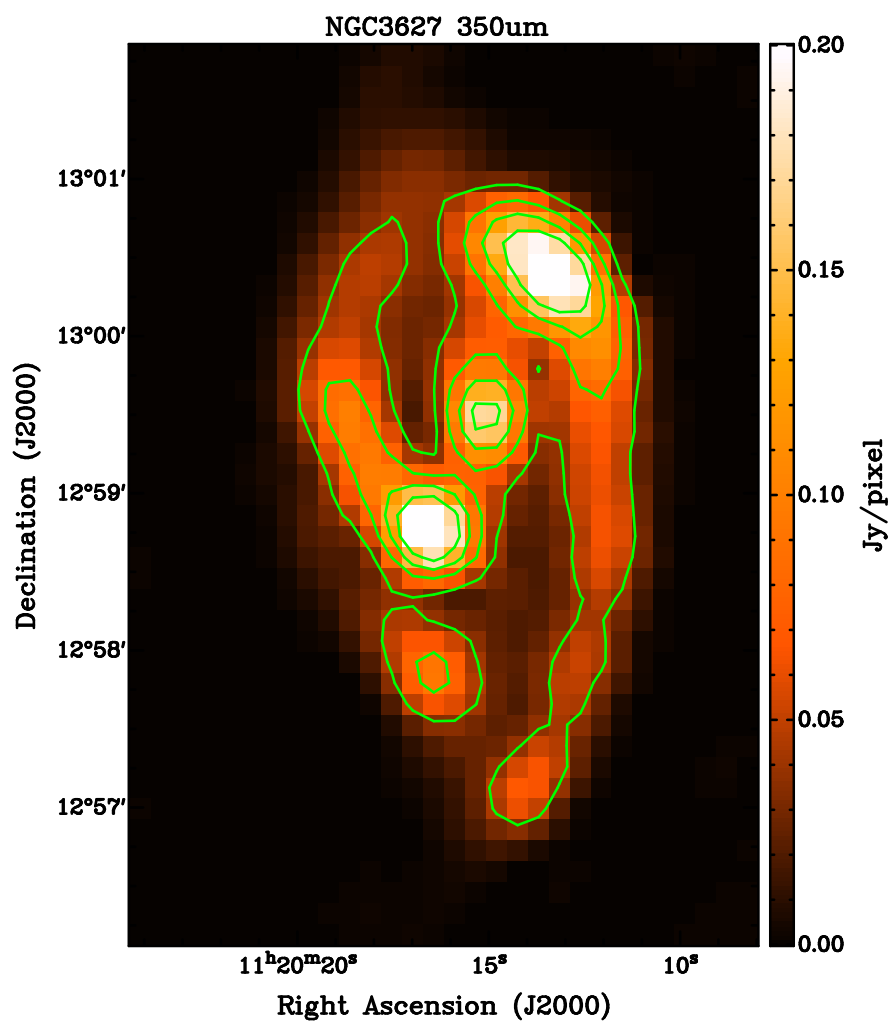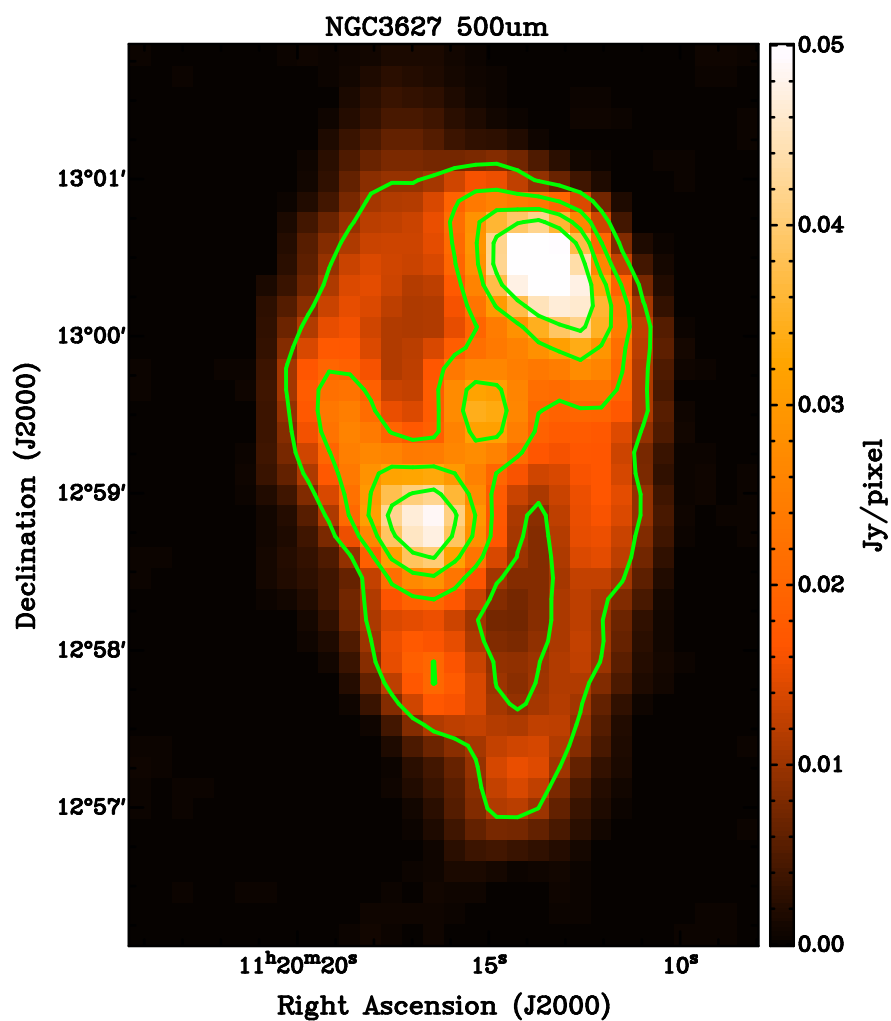Figure 2.10: Image after the MAKEMAP filtering of the 350μm observations with 20%, 40%, 60%, and 80% contours.

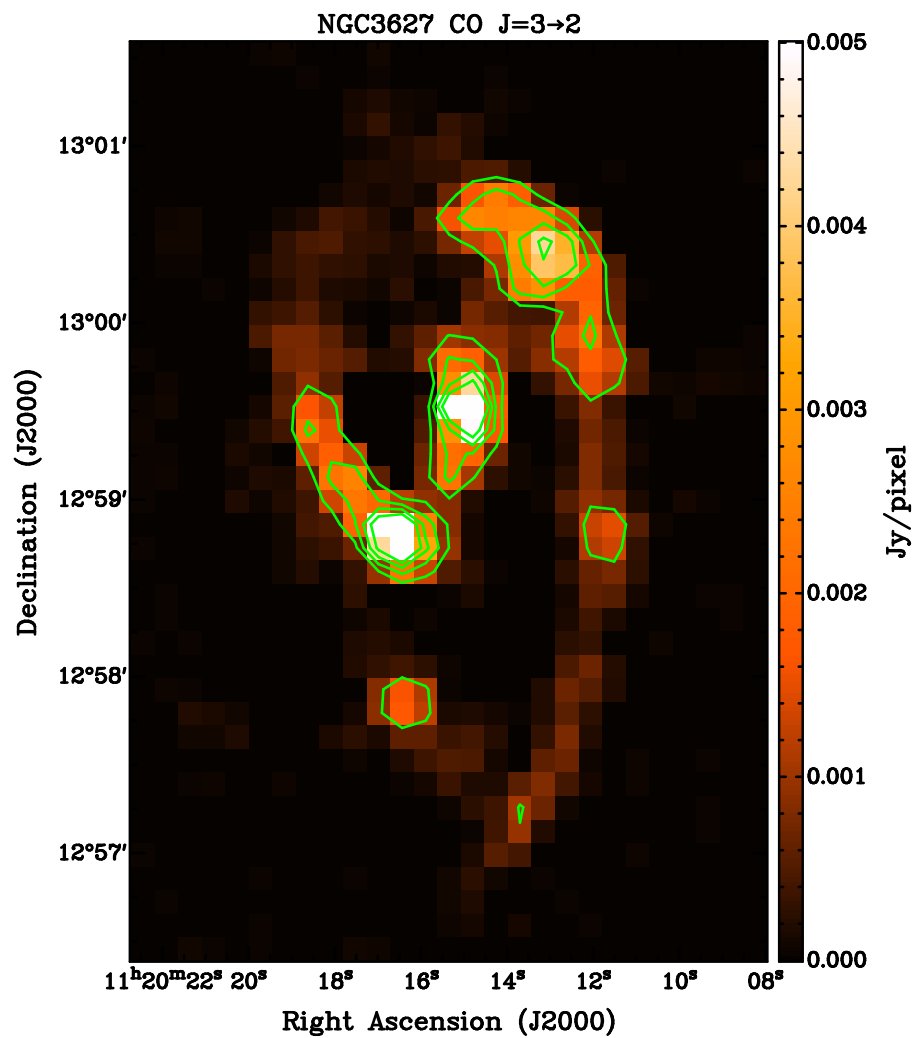Figure 2.11: Image after the MAKEMAP filtering of the 500μm observations with 20%, 40%, 60%, and 80% contours.

Figure 2.12: Residual of the MAKEMAP filtering of CO J=3-2 observations used to subtract line contamination from $850\mu m$ SCUBA-2 map with 20%, 40%, 60%, and 80% contours.

Table 2.4.   Properties of NGC3627 Nobeyama 45-m Observations

Observation	Beam Properties θ_{beam}	RMS [K km/s]	Percentage of Emission Removed
CO J=1-0	15.0″	0.681	20%

2.3.3 Nobeyama 45-m

Determining a dust-to-gas ratio requires a molecular tracer to estimate the amount of molecular hydrogen present. The most frequently used tracer is CO J=1-0 due to its abundance in the ISM. The CO J=1-0 we used was taken from the Nobeyama 45-m CO Atlas of Nearby Spiral Galaxies observed to better understand the role of bars relating to molecular gas (Kuno et al., 2007). The Nobeyama 45-m CO Atlas consists of galaxies with morphologies ranging from Sa to Scd, located less than 25Mpc from the Milky Way, inclination values greater that 79°, 100μm flux greater than 10Jy, and spiral structure that has not be comprimised through interactions. Any galaxies that met this criteria were then observed with the Nobeyama 45-m telescope (Kuno et al., 2007). The beam sizes and rms of the filtered CO J=1-0 map are displayed in table 2.4 and the final image product can be seen in figure 2.13.

2.3.4 Hetrodyne Reciever Array CO-Line Extragalactic Survey (HER-ACLES)

The CO J=2-1 line was used to determine a CO $2-1/1-0$ line ratio which can be used to trace a gradient in α_{CO} and hint towards regions of
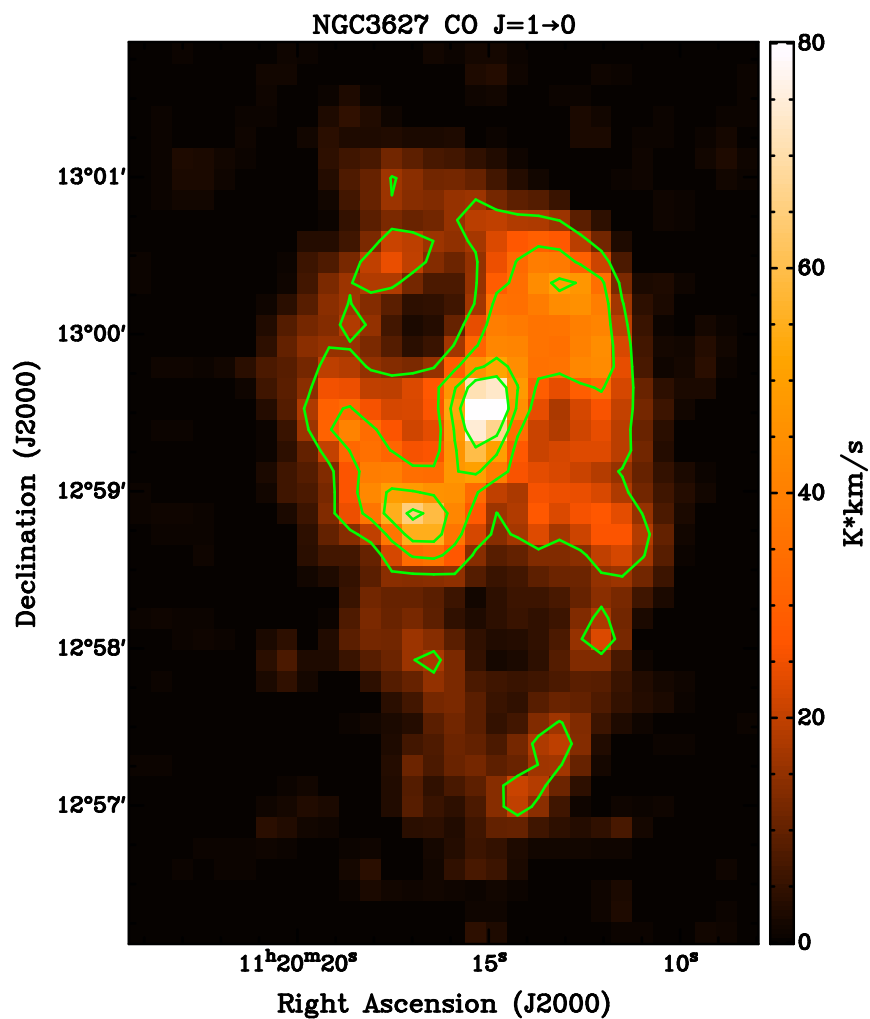
Figure 2.13: Residual of the MAKEMAP filtering of CO J=1-0 observations with 20%, 40%, 60%, and 80% contours.

Table 2.5.   Properties of NGC3627 HERACLES Observations

Observation	Beam Properties θ_{beam}	RMS $[K\ km/s]$	Percentage of Emission Removed
CO J=2-1	13.0″	0.305	7%

high star-formation (Reuter et al., 1996). We used the CO J=1-0 data from the Nobeyama 45-m telescope (§ 2.3.3), and CO J=2-1 from the Hetrodyne Reciever Array CO-Line Extragalactic Survey (HERACLES) using the IRAM 30-m telescope. The main goal of HERACLES was to quantify the relationship between atomic and molecular gas and star formation using a large sample of galaxies (Leroy et al., 2009). The sample of galaxies chosen were targets contained in THINGS that were within the observing limits of the IRAM 30-m telescope. The final image can be seen in figure 2.14 and the image properties can be seen in table 2.5.

2.3.5 The HI Nearby Galaxy Survey (THINGS)

To determine the gas to dust ratio we had to determine the total amount of gas present which includes both atomic and molecular hydrogen. We approximated the amount of molecular hydrogen by using CO J=1-0, and measured the amount of atomic hydrogen (HI) present. The source of our atomic hydrogen came from The HI Nearby Galaxy Survey (THINGS) designed to observe HI emission in nearby galaxies with the extreme spatial resolution of the Very Large Array (VLA). Targets in THINGS included many of the SINGS targets
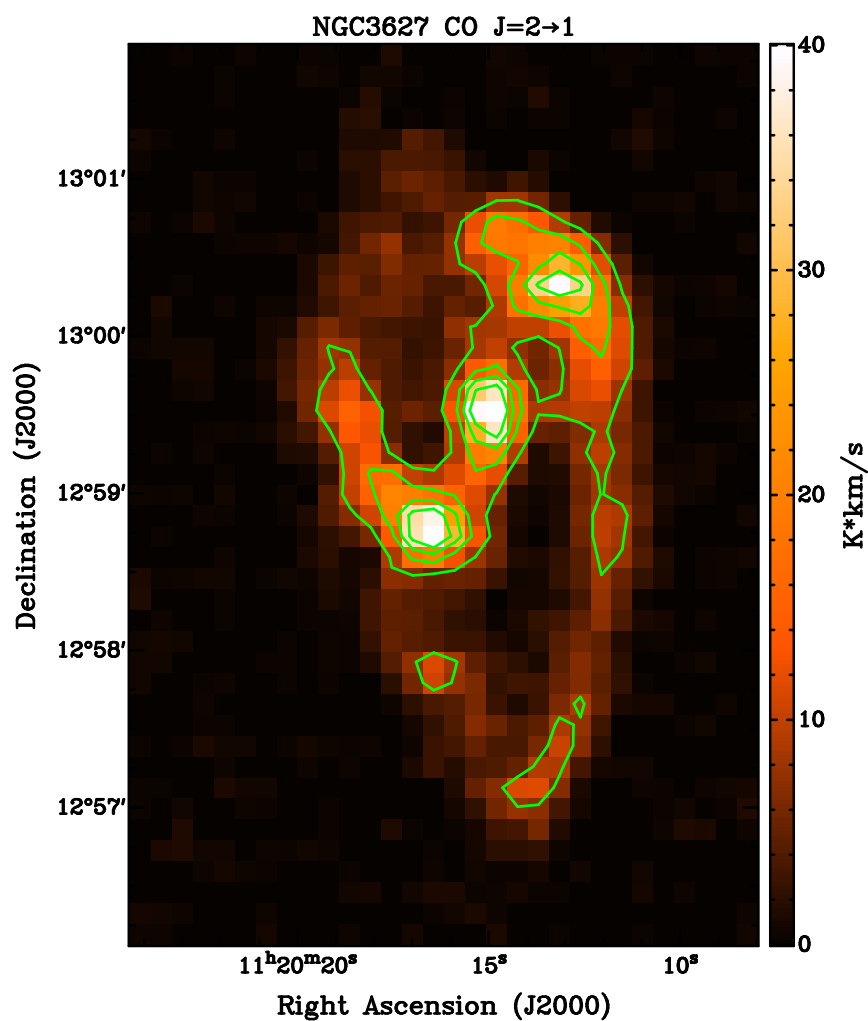
Figure 2.14: Residual of the MAKEMAP filtering of CO J=2-1 observations with 20%, 40%, 60%, and 80% contours.

Table 2.6.   Properties of NGC3627 THINGS Observations

| Observation | Beam Properties | | | RMS | Percentage of Emission Removed |
	θ_{maj}	θ_{min}	θ_{PA}	$[M_\odot/pc^2]$	
HI	10.6″	8.85″	-48.0°	0.760	¿99%

with the exception of known HI poor sources (E/S0 type galaxies), dynami-
cally complex systems (edge-on spirals), and large extended galaxies found in
the Local Group (Walter et al., 2008). The resolution and rms of the filtered
image are shown in table 2.6. The final data product is shown in figure 2.15
which has been converted to $M_\odot$ pc^{-2} using equation 2.2 in Walter et al. (2008)
divided by the pixel area in pc^2 such that D is the distance, and $\sum_i S_i \Delta v$ is
the first moment of the flux.

$$M_{HI}[M_\odot] = 2.36 \times 10^5 D^2 \times \sum_i S_i \Delta v \tag{2.2}$$

2.4 Data Preparation for Analysis

Initially the data do not agree on several levels. The differences consist
of the presence of the large scale/extended structure and different resolutions
including the beam shape of the 450μm. We have taken several steps to correct
these disagreements and maximize the compatibility of the data. In order to
account for the varying beam resolutions, we use a gaussian convolution to
increase the resolution of our maps to the largest beam size in our dataset,
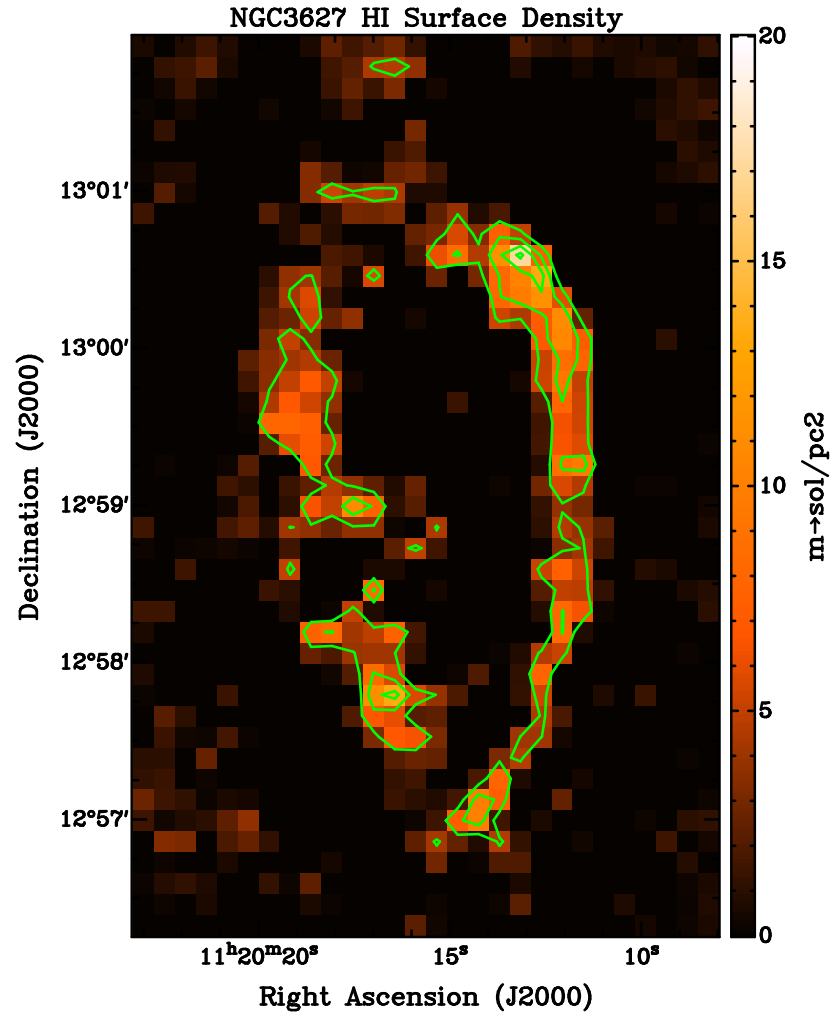σ_{max}=36″. We use equation 2.3 to decide on an appropriate convolution beam

Figure 2.15: Residual of the MAKEMAP filtering of HI observations with 20%, 40%, 60%, and 80% contours.

size such that σ_{desire} is the desired beam width, σ_{max} is the beam size we are convolving to, and σ_{given} is the beam size we are convolving from.

$$\sigma_{desire} = \sqrt{\sigma_{max}^2 - \sigma_{given}^2} \tag{2.3}$$

However, this only works when the beams are well approximated by a gaussian which is not the case for the 450μm beam. The steps taken to match the resolution of the 450μm beam with the rest of the data set are given in § 2.4.1. Removing any large scale structure from our ancillary data is implemented using a feature built into MAKEMAP that allows us to add fake sources into the data during production. The fake source implementation allows us to remove the same amount of large scale structure from our ancillary data as was removed from the SCUBA-2 data. The steps taken to prepare the ancillary data are described in §2.4.2.

2.4.1 Accounting for the 450μm Error Beam

Taking the 450μm error beam into consideration is different than a normal beam convolution in the sense that we are not convolving the higher resolution map to the lowest resolution. Instead we are adding in an error beam similar to the error beam found in the 450μm observations. We have to take these steps because convolving a double gaussian beam with a single gaussian kernel will not sufficiently remove the error component of our beam resulting in a poor approximation to the wings of our beam shape.

In order to accommodate the 450μm map's error beam, we used a method employed by another SCUBA-2 survey, the Gould Belt Survey team. This method used the distributive nature of the Fourier transform to create similar error components in the beams we were convolving to and from. Carrying out this convolution involved breaking the 450μm beam into its two components, X_α and X_β to represent the main beam and error beam. The values of the main beam amplitude, X_α, and error beam amplitude, X_β, will sum to one so the height of the total beam is normalized to one. The poorest resolution beam, X_{max}, is convolved with the two components X_α and X_β and the resulting beams are added together. This process produces an equivalent two component beam as the 450μm beam convolved with X_{max}. This relationship is shown in equation 2.4, where X_{max} is the poorest resolution beam, X_α and X_β are the main and error beam of the 450μm observations, and $X_{450\mu m}$ is the double gaussian beam shape of the 450μm observations.

$$
\begin{aligned}
X_{max} * X_\alpha + X_{max} * X_\beta &= (X_\alpha + X_\beta) * X_{max} \\
&= X_{450\mu m} * X_{max}
\end{aligned}
\tag{2.4}
$$

2.4.2 Extended Structure Removal via MAKEMAP

Due to the combination of methods used in MAKEMAP, large scale/extended structure is removed from the final SCUBA-2 images. However, in all of our ancillary data the large scale emission was present in the initial maps. The removal of the extended features from our support data was carried out by passing the data through MAKEMAP using a special function called fakemap.

Implementing fakemap allows us to pass an image though processing and have it added into the image being processed. We use the 850μm map as our base image for the filtering process and add the ancillary data to the image. The output image then consists of the sum of the ancillary data and the 850μm map. The ancillary data were then isolated by subtracting the 850μm image from the fakemap image.

Preparing the data to be implemented consisted of either converting the images from their native units into pW using the 850μm flux calibration factor and scaling down to match the observed signal or by just applying a scaling factor. Which method is used is based on the desired units of the final map, and can be separated by what purpose the data had in our analysis.

The data used in the SED fitting (KINGFISH and NGLS) were scaled to pW so they could have a similar reduction and calibration process as the SCUBA-2 maps. The KINGFISH data is regridded to a $2''$ by $2''$ pixel size and has the appropriate calibration factor from Dempsey et al. (2013) applied to convert from either MJy/sr to pW in the case of the 250μm, 350μm, and 500μm or from Jy/pixel to pW for the 100μm and 160μm. Converting the CO J=3-2 requires the final product to be in the same units as the 850μm observations in order to properly remove its molecular gas contribution. Converting from K km/s to mJy/beam involved applying a scaling constant of 0.70 [mJy/beam][K km/s]$^{-1}$ (Drabek et al., 2012) prior to applying the 850μm flux calibration factor to convert to pW. After the data has been converted to pW, the image used as a fakemap is then scaled down to the same order of magnitude as the base image using a scaling factor specified prior to the map production.

After the fakemap image has been processed and the 850μm map subtracted, the maps are scaled back up using the scaling factor used to scale them down and calibrated using the same flux calibration factors as the 850μm map and scaled to an $8''$ by $8''$ grid. The amount of extended flux lost in the KINGFISH and NGLS is shown in tables 2.2 and 2.3. This process is shown in figure 2.16 from the original Herschel 100μm map, to the final image used in SED fitting convolved to the 500μm beam resolution, $36.0''$.

The rest of the ancillary data is used in calculating a dust to gas ratio, and follows nearly the same process as the SED data filtering. The major difference is the CO J=1-0, CO J=2-1 and HI maps need to remain in their original units of K km/s and $M_\odot/pc^2$. This necessity simplified the process by only requiring a scaling factor of 0.001 to be applied to the original maps. After the data is scaled, it is filtered using the fakesource option in MAKEMAP with the 850μm observation as the base image. The atomic and molecular gas maps were then isolated in the same fashion as the KINGFISH and NGLS, however they were rescaled back to their original values and fit to an $8''$ by $8''$ grid then finally convolved to a $36.9''$ resolution. The process is shown in figure 2.17. The amount of emission lost is shown in tables 2.4, 2.5, and 2.6.
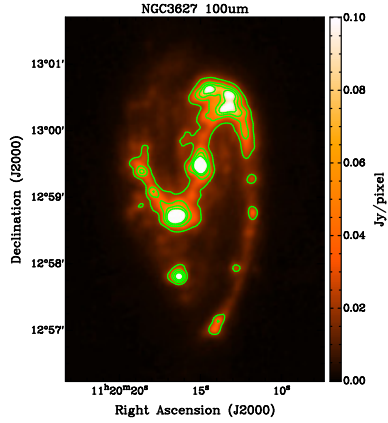
(a) Herschel 100μm image of NGC3627.
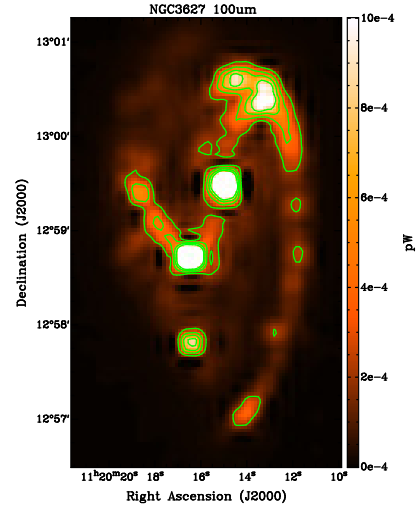
(b) Herschel 100μm image converted to pW and rescaled to a $2''$ by $2''$ pixel grid.
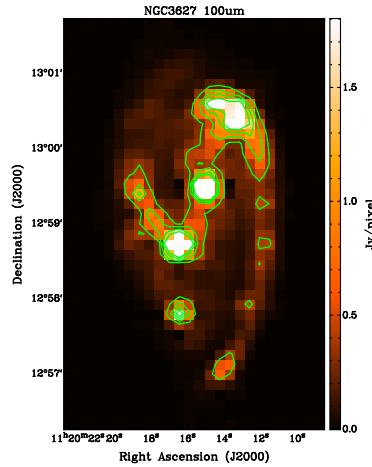
(c) 100μm map of NGC3627 after large scale structure has been removed on an $8''$ by $8''$ grid.
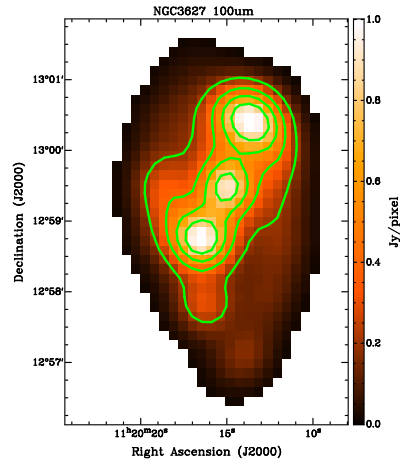
(d) 100μm map with extended structure removed and convolved to final resolution of $36.0''$ with a 5σ cut applied.

Figure 2.16: The 100μm image from the beginning of processing to the end of processing. All of the contours shown are 20%, 40%, 60%, and 80%.
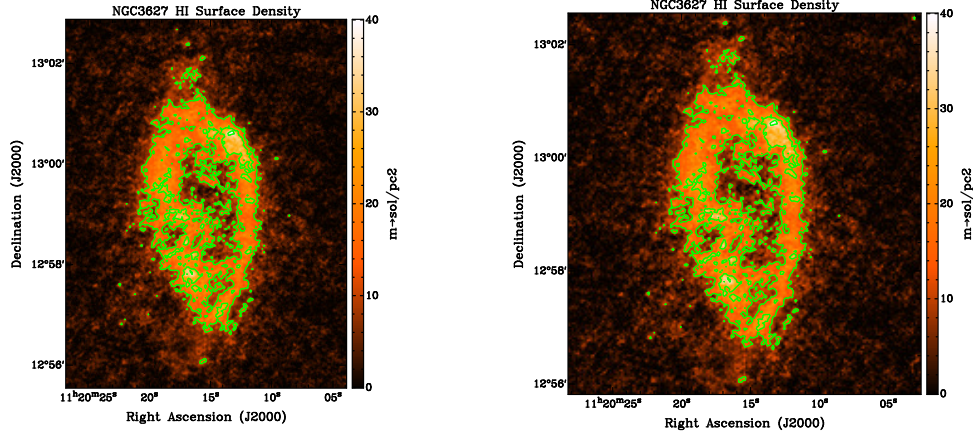
(a) HI surface density map of NGC3627.

(b) HI surface density map rescaled to a 2″ by 2″ pixel grid.
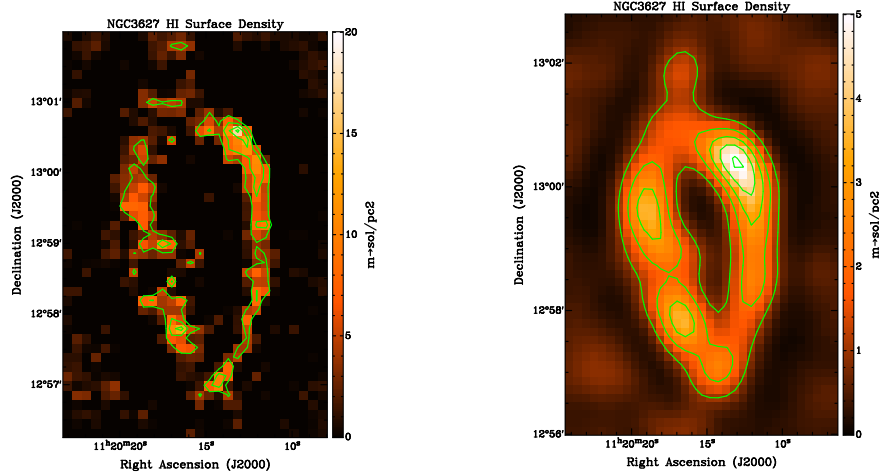
(c) HI surface density map of NGC3627 after large scale structure has been removed on an 8″ by 8″ grid.

(d) HI surface density map with extended structure removed and convolved to final resolution of 36.0″.

Figure 2.17: The HI surface density maps from the beginning of processing to the end of processing. The contours in the top row are 30%, 60% and 90%, and the contours in the bottom row are 20%, 40%, 60%, and 80%.

Chapter 3

Spectral Energy Distribution Analysis

3.1 SED Fitting Method

In order to determine a dust mass, we use the IDL package MPFIT (Markwardt, 2009) to fit equation 3.1 for the temperature, T, mass, M, and the emissivity index, β. The routine MPFIT utilizes the Levenberg-Marquardt algorithm. This algorithm uses a combination of two minimization techniques (the steepest descent method and the Newton-Raphson Method) to determine the parameter combination that corresponds to a minimum in the χ^2 space while maximizing the efficiency of the step sizes in each iteration (Burden & Faires, 2001). The algorithm begins by implementing the steepest descent method. This working of this technique is to follow the direction opposite of the largest gradient in order to traverse the χ^2 space to locate a minimum. As the set of solutions approaches a minimum, it will switch to the Newton-Raphson method to locate the best set of parameters by finding where the derivative at that point is closest to zero (Gavin, 2013).

Table 3.1.   Calibration Factors for SCUBA-2 and KINGFISH Observations

Observation	Scaling Factor
100μm	0.03
160μm	0.05
250μm	0.07
350μm	0.07
450μm	0.12
500μm	0.07
850μm	0.08

$$S_\nu\left(T\right) = \frac{M\,\kappa_{\nu,0}}{D^2}\left(\frac{\nu}{\nu_0}\right)^{\beta+3} B_\nu\left(T\right) \tag{3.1}$$

In order for MPFIT to provide the most accurate fit, we establish a reasonable error for each of our data points, and determine a realistic set of starting points for the fitting. The variance for our SCUBA-2 data is determined by equation 3.2 such that σ_{obs} is the noise determined by MAKEMAP, $\sigma_{rms,sky}$ is the RMS of the sky, and σ_{calib} is the calibration uncertainties where the scaling factor is shown in table 3.1.

$$\sigma^2 = \sigma_{obs}^2 + \sigma_{rms,sky}^2 + \sigma_{calib}^2 \tag{3.2}$$

The variance for the KINGFISH data are determined in a similar fashion and are shown in equation 3.3, however the observation error is excluded since the reported variance in the filtered images are reflective of the fake source image used and not of the KINGFISH data set.

$$\sigma^2 = \sigma^2_{rms,sky} + \sigma^2_{calib} \tag{3.3}$$

The nature of the Levinberg-Marquardt method leaves the solution vulnerable to converge at a local minimum rather than converging at the global minimum. This is remedied by selecting reasonable initial conditions. The initial conditions we used were a modified blackbody with a temperature of 20K, a dust emissivity index of 2, and a mass determined by equation 3.4 using the flux from the 250μm emission and our initial temperature and dust emissivity values.

$$\begin{aligned} M &= \frac{D^2\,I_{250}}{\kappa_{\nu,0}\,B_{250}\left(T\right)} \left(\frac{\nu}{\nu_0}\right)^{-(\beta+3)} \\ &= 2.24 \times 10^5\,I_{250}\ [M_\odot] \end{aligned} \tag{3.4}$$

3.2 Fitting the Spectral Energy Distribution

The fitting procedure was carried out in two different ways on a modified blackbody equation, equation 3.1. One of the two methods is fitting an SED to each individual pixel in order to generate a set of parameter maps, and the second is by totaling the flux of each of the selected regions shown in figure 3.1 to maximize the signal to noise ratio in order to generate a more precise set of parameters. For both of the fitting methods the mass, M, and temperature, T, are set as free parameters, but the treatment of the emissivity index, β, required special treatment for each of the methods. The distance, D, has been set to 9.4 Mpc (Walter et al., 2008), and the reference opacity,

$\kappa_{\nu,0}$, was tested using 0.2665 m^2 kg-1 (Li & Draine, 2001) and 1.0 m$^-$2 kg$^-$1 (Planck Collaboration et al., 2011).

3.2.1 Pixel SED Fits

In order to generate a parameter map of NGC3627, each individual pixel has it's own SED determined from the available wavelengths described in the observations chapter. Initially, we exclude the 500μm emission, and in later fits, we substitute the 450μm emission with 500μm emission. The treatment of the dust emissivity index is performed by fixing it at $\beta = 1.8$ for the Planck opacity model such that the opacity is $\kappa_{300\mu m,0} = 1.0$ m^2 kg^{-1} (Planck Collaboration et al., 2011) and $\beta = 2.0$ for the Li and Draine opacity model where the opacity is $\kappa_{300\mu m,0} = 0.2665$ m^2 kg^{-1} (Li & Draine, 2001). A third fit is performed where the emissivity index is allowed to vary as a free parameter. While the emissivity index is allowed to vary, the opacity being used is the Planck model in order to generate a minimum mass estimate of the two opacity values. Using either an opacity of 1.0 m^2 kg^{-1} or 0.2665 m^2 kg^{-1} will not effect the shape of the SED, only the its normalizing value. In the case of our fits, it is the mass that acts as the normalizing constant, so increasing or decreasing the opacity will yield the opposite effect in the mass. The inverse proportionality can be seen in equation 3.4. The resulting parameter maps of the fits are shown in figure 3.2. The numerical values from fitting each model are shown in tables 3.2, 3.3, and 3.4 where each region corresponds to the regions labeled in figure 3.1.
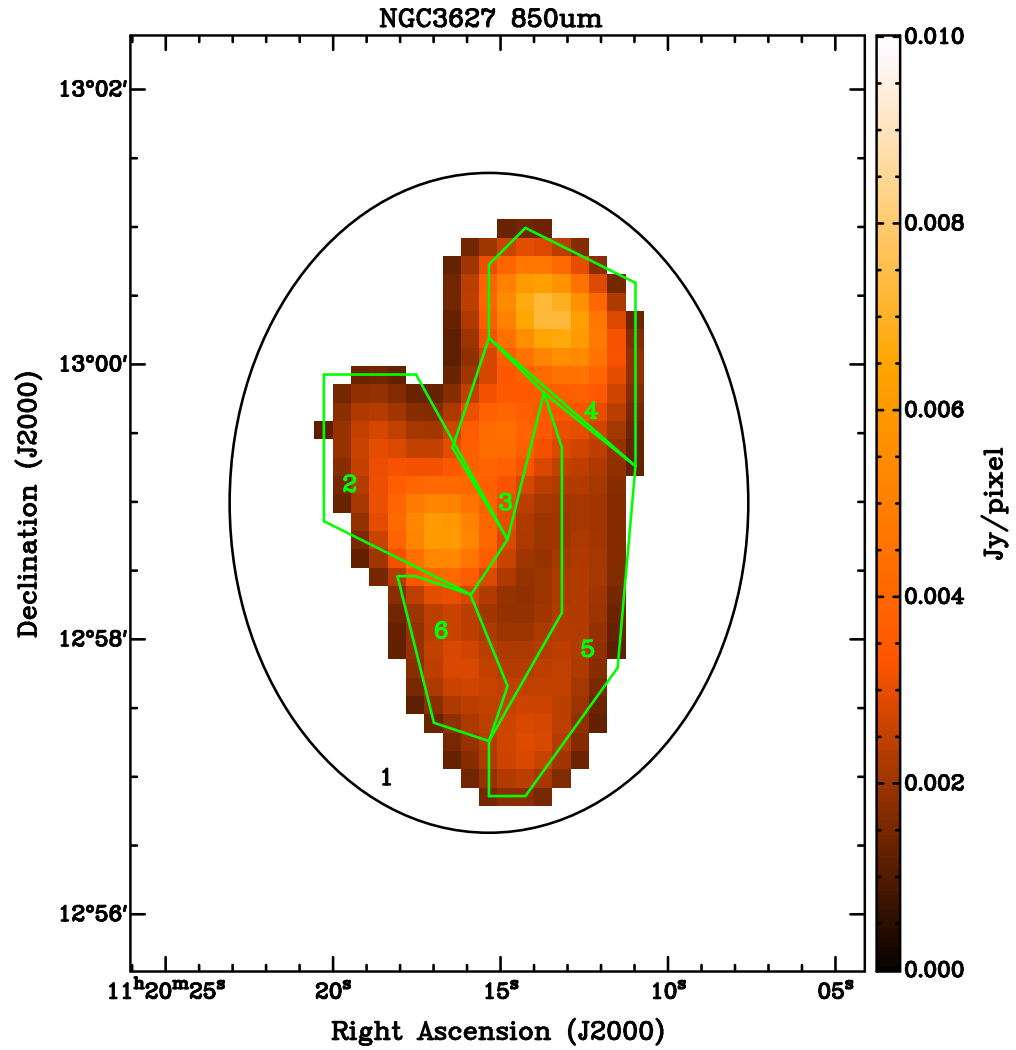
Figure 3.1: 850μm emission convolved to the 500μm beam size overlaid with the selected regions of NGC3627 labeled 1 through 6 such that region 1 includes the entire galaxy.
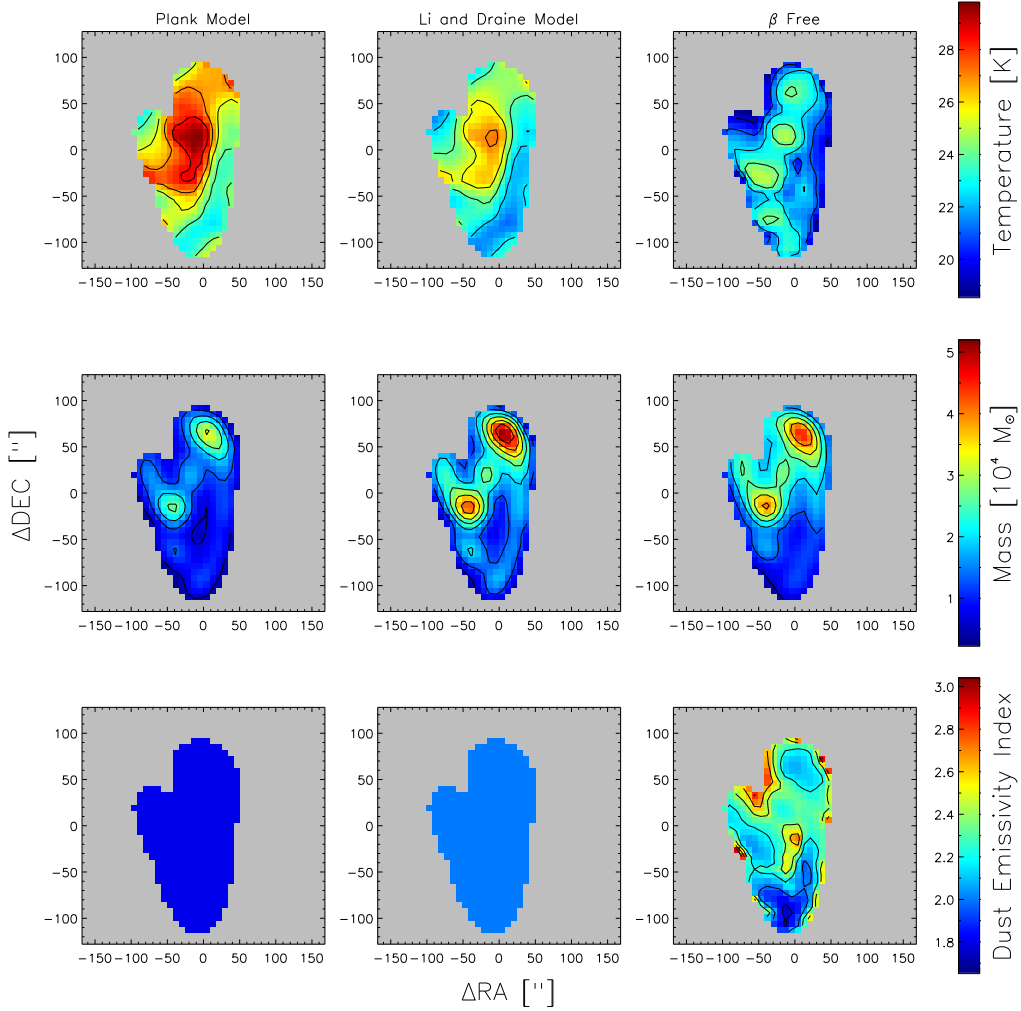
Figure 3.2: Returned value for the SED fits with the Planck model in the left column, the Li and Draine model in the middle column, and β as a free variable in the right column. The top row shows the temperature with contours from 1.5K to 28.5K in 1.5K increments. The second row show the returned masses with contours from $1.9M_\odot$ to $13.3M_\odot$ in $1.9M_\odot$ increments. The Li and Draine mass fits have been divided by three to better show the features. Th bottom row shows the returned dust emissivity index values with contours from 1.8 to 2.8 with 0.2 increments.

Table 3.2.   Best Fit Parameters for Planck Model

Region	Average β	Total Mass $[10^5 M_\odot]$	Surface Density $[M_\odot pc^{-2}]$	Average Temperature [K]
1	1.8	47 ± 22	0.09 ± 0.04	26 ± 2
2	1.8	12 ± 4	0.11 ± 0.04	27 ± 2
3	1.8	5 ± 1	0.10 ± 0.02	28.8 ± 0.6
4	1.8	14 ± 5	0.14 ± 0.05	26 ± 1
5	1.8	9 ± 2	0.07 ± 0.02	24 ± 1
6	1.8	3.8 ± 0.9	0.07 ± 0.02	25 ± 1

Table 3.3.   Best Fit Parameters for Li and Draine Model

Region	Average β	Total Mass $[10^5 M_\odot]$	Surface Density $[M_\odot pc^{-2}]$	Average Temperature [K]
1	2.0	219 ± 103	0.4 ± 0.2	24 ± 2
2	2.0	54 ± 19	0.5 ± 0.2	25 ± 1
3	2.0	26 ± 5	0.48 ± 0.09	26.4 ± 0.5
4	2.0	67 ± 23	0.7 ± 0.2	24.4 ± 0.8
5	2.0	40 ± 9	0.33 ± 0.07	22.4 ± 0.9
6	2.0	17 ± 4	0.32 ± 0.08	23.5 ± 0.9

Table 3.4.   Best Fit Parameters for β As A Free Parameter

Region	Average β	Total Mass $[M_\odot]$	Surface Density $[10^5 M_\odot pc^{-2}]$	Average Temperature [K]
1	2.2 ± 0.2	73 ± 35	0.14 ± 0.06	22 ± 1
2	2.3 ± 0.2	19 ± 6	0.18 ± 0.05	22 ± 2
3	2.34 ± 0.09	9 ± 1	0.18 ± 0.02	23.0 ± 0.9
4	2.2 ± 0.1	22 ± 6	0.21 ± 0.05	22 ± 1
5	2.1 ± 0.2	12 ± 4	0.10 ± 0.03	22 ± 1
6	2.1 ± 0.1	5 ± 1	0.09 ± 0.02	23.0 ± 0.9

The wellness of each fit is shown figures 3.3, 3.4, and 3.5 for the Plank model, Li and Draine model, and beta as a free parameter respectively. The quality of the fit is determined by how well the expected flux from the SED fitting matches the observed flux. If the fits are able to recreate the observed emission, then all of the points will lie on the line $y = x$ shown in the plots as a black line. If the SED is underestimating the flux, the points will appear below the 1 to 1 line, and an over estimation from the SED will result in points above the line.

Using these plots, it is clear that the SED is over estimating the 450μm flux despite the care taken while accounting for the odd beam shape of the 450μm data. This overestimation was not a result of a poor fit, but rather a calibration error in the 450μm observations. The intrinsic error to the SCUBA-2 450μm data was determined by extrapolating an expected value from the 350μm and 500μm KINGFISH data assuming the decrease in intensity was linear. In order to avoid any errors in our final parameter maps, we substitute the 450μm emission with KINGFISH 500μm emission. The quality of fit maps using the 500μm emission are shown in figures 3.6, 3.7, and 3.8 for the Planck model, Li and Draine model and the emissivity as a free parameter respectively. To assign a numerical quantity to the vertical distance was calculated for each point to the 1 to 1 line and then summed. The summed distances are shown in table 3.5 and suggest the best fit comes from allowing the emissivity index to vary.
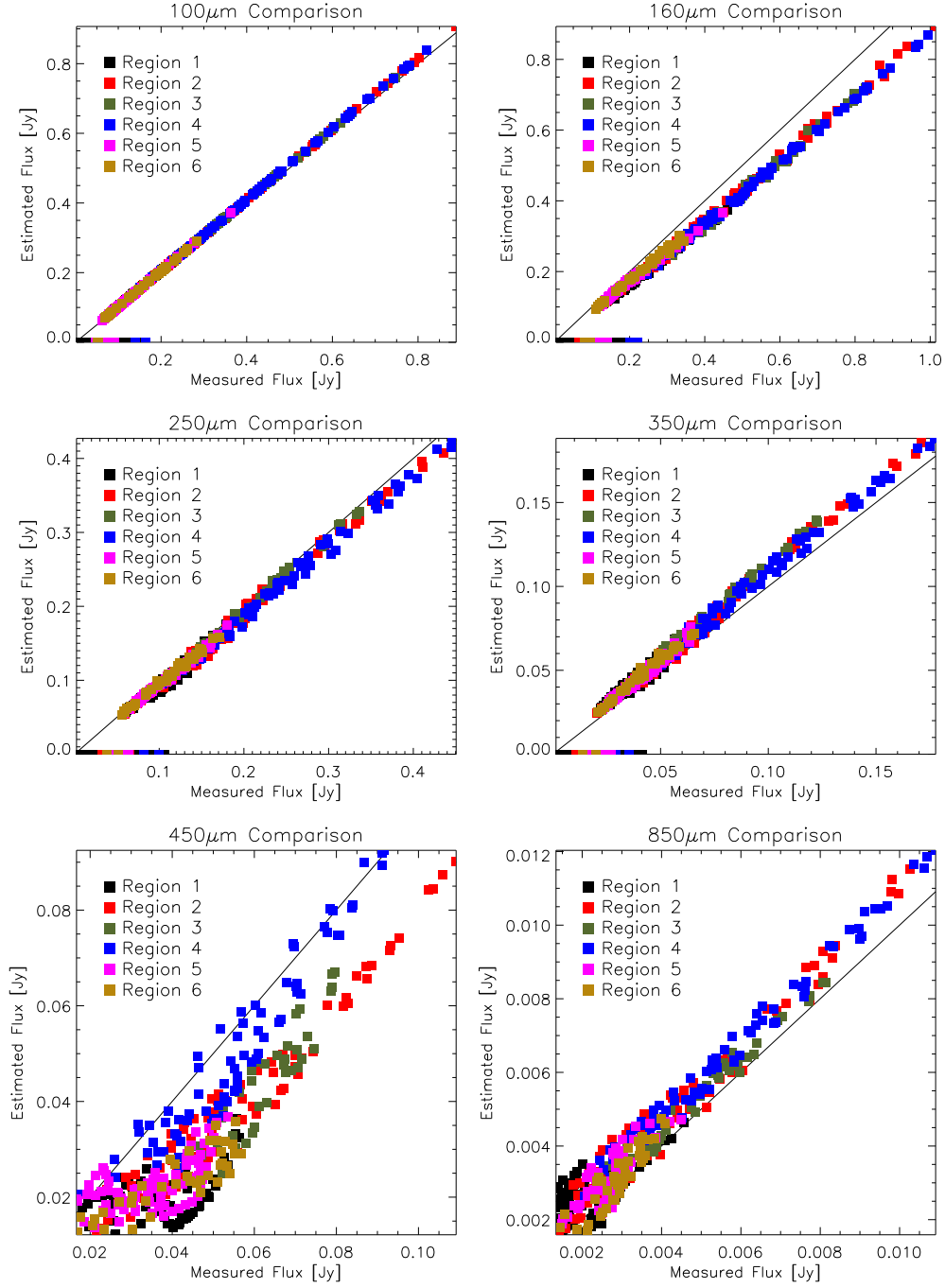
Figure 3.3: Quality of the SED fits to the Planck model using the 450μm emission. The regions shown are the regions in figure 3.1.
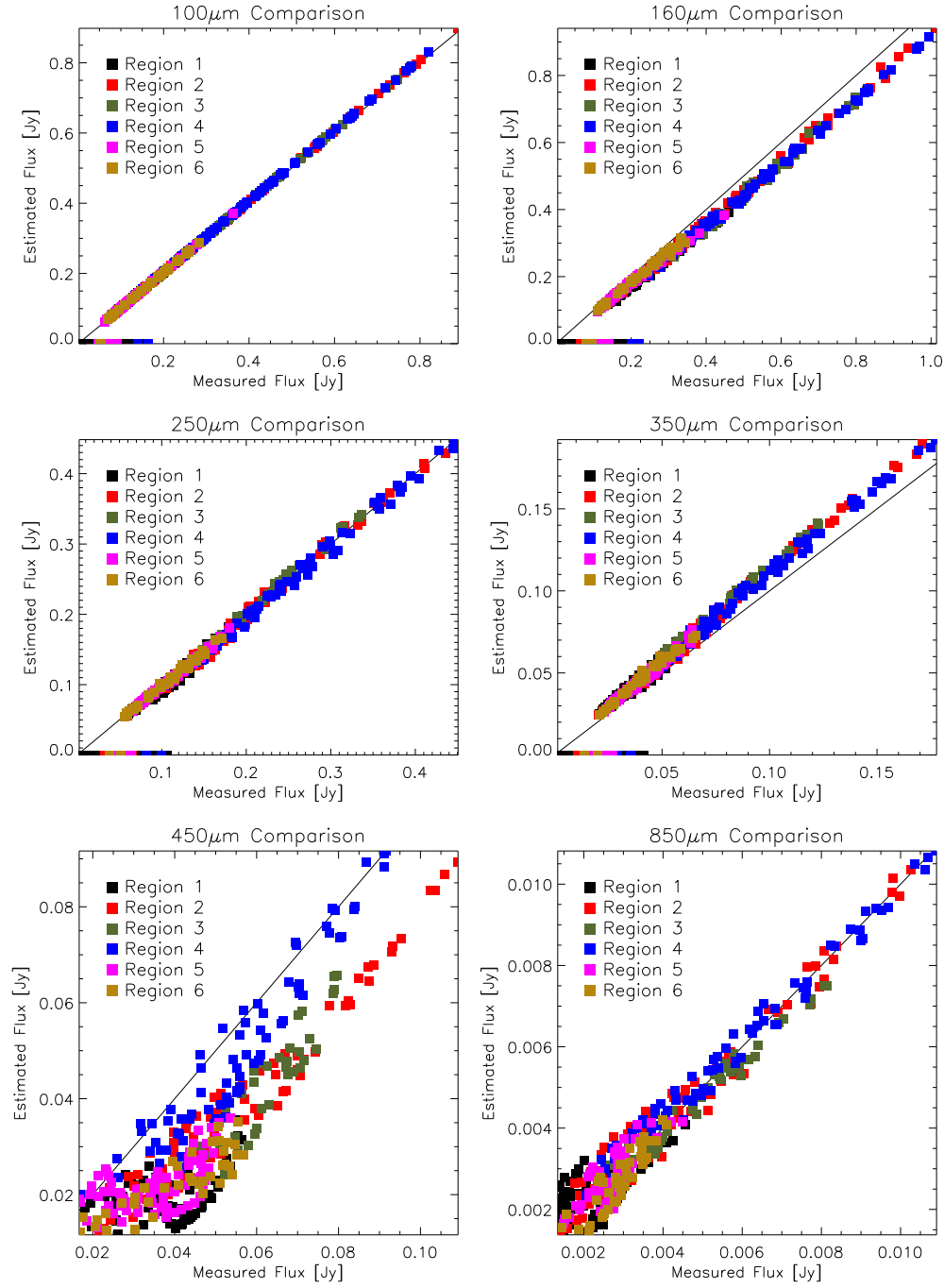
Figure 3.4: Quality of the SED fits to the Li and Draine model using the 450μm emission. The regions shown are the regions in figure 3.1.
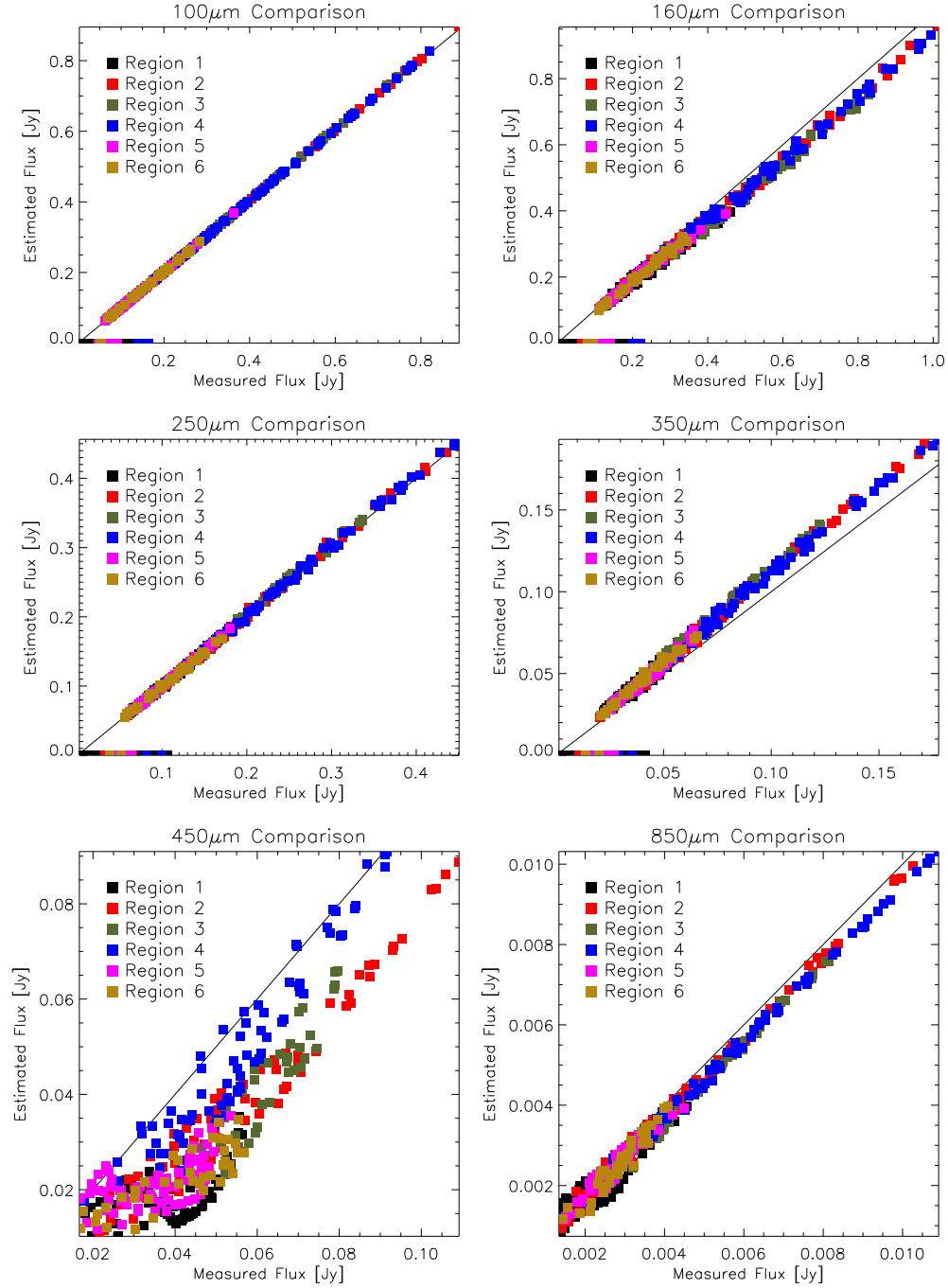
Figure 3.5: Quality of the SED fits with the dust emissivity index as a free parameter using the 450μm emission. The regions shown are the regions in figure 3.1.

Figure 3.6: Quality of the SED fits using to the Planck model with the 500μm emission. The regions shown are the regions in figure 3.1.
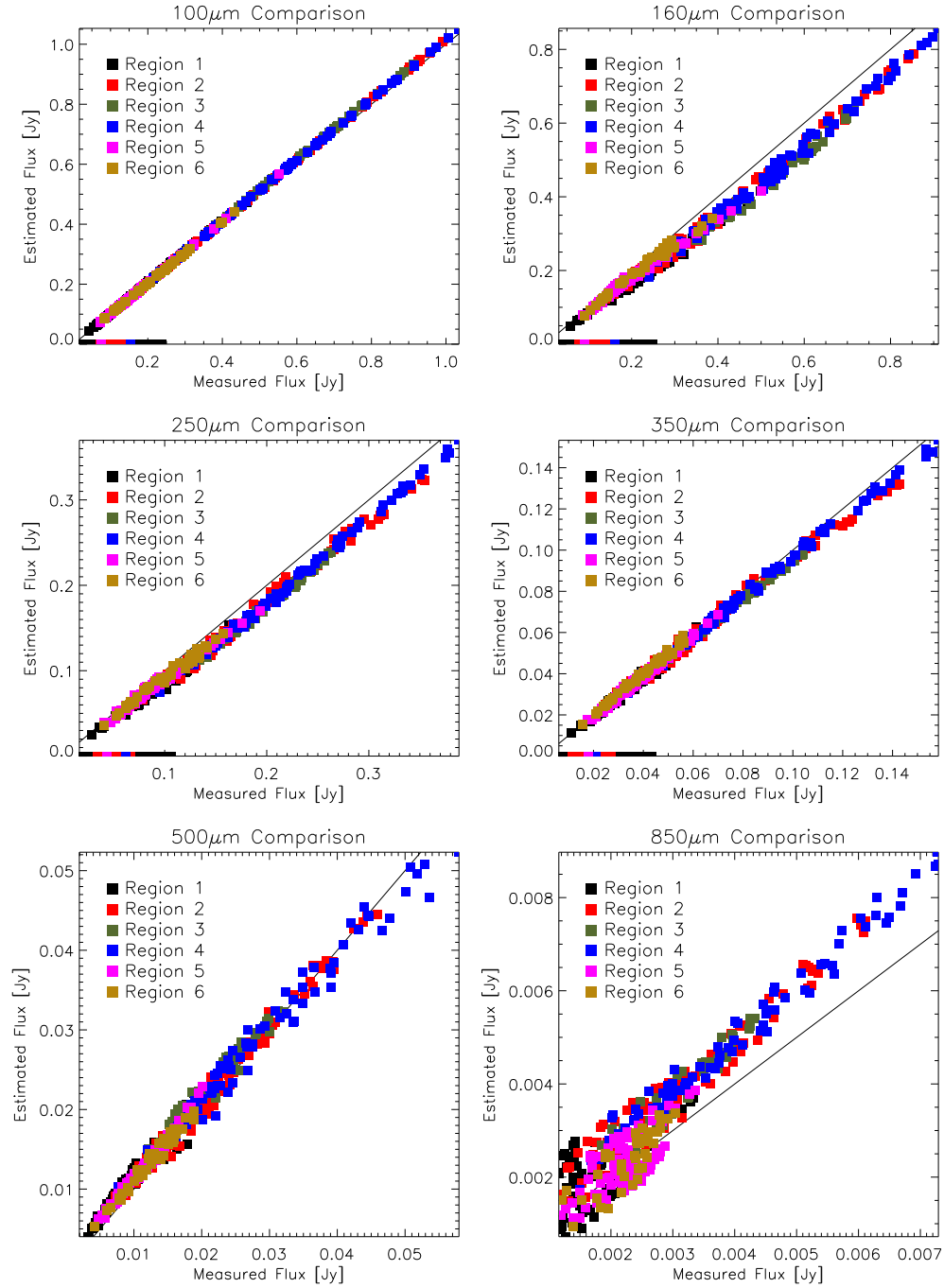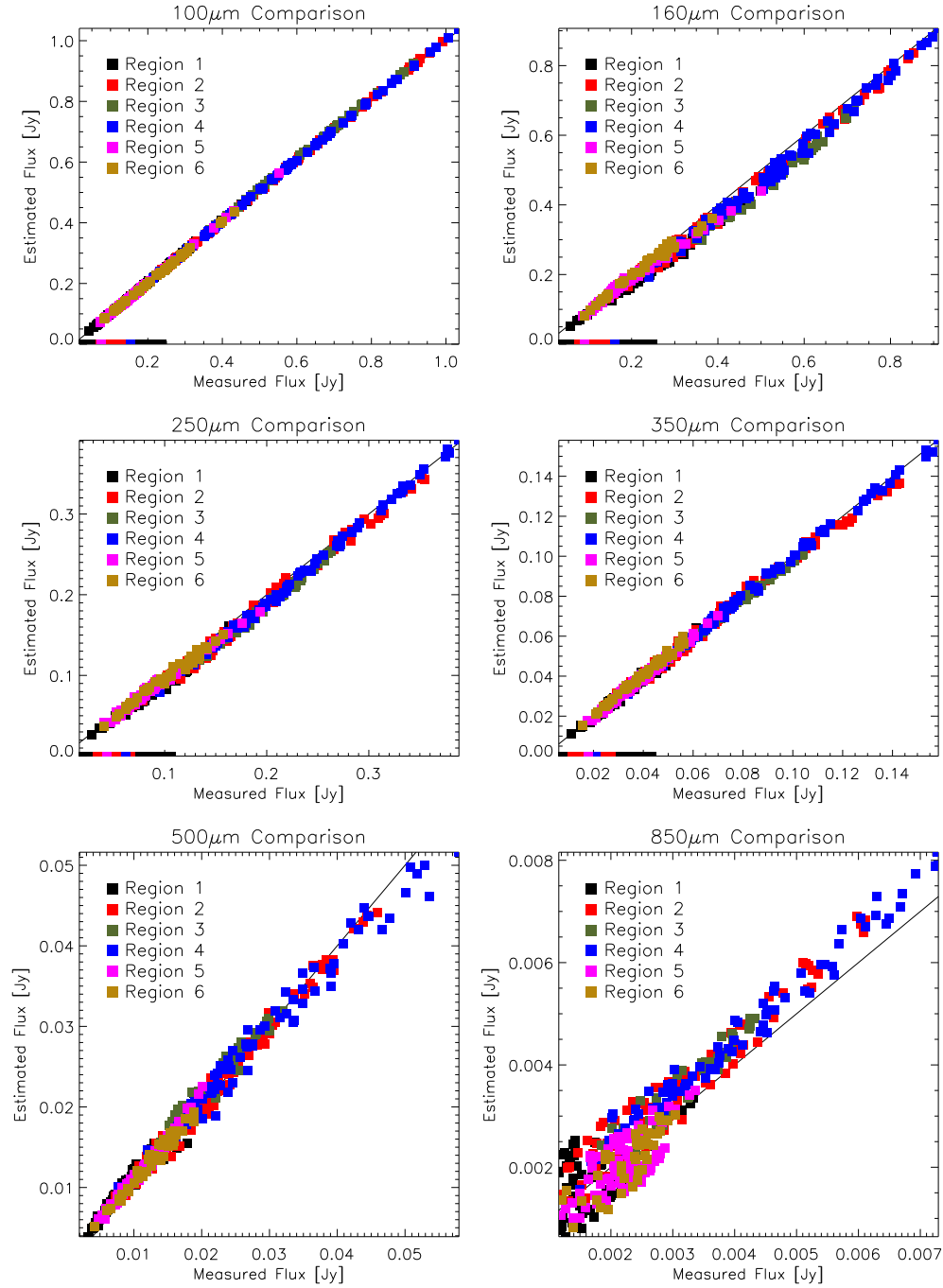
Figure 3.7: Quality of the SED fits using the Planck model with the 500μm emission. The regions shown are the regions in figure 3.1.
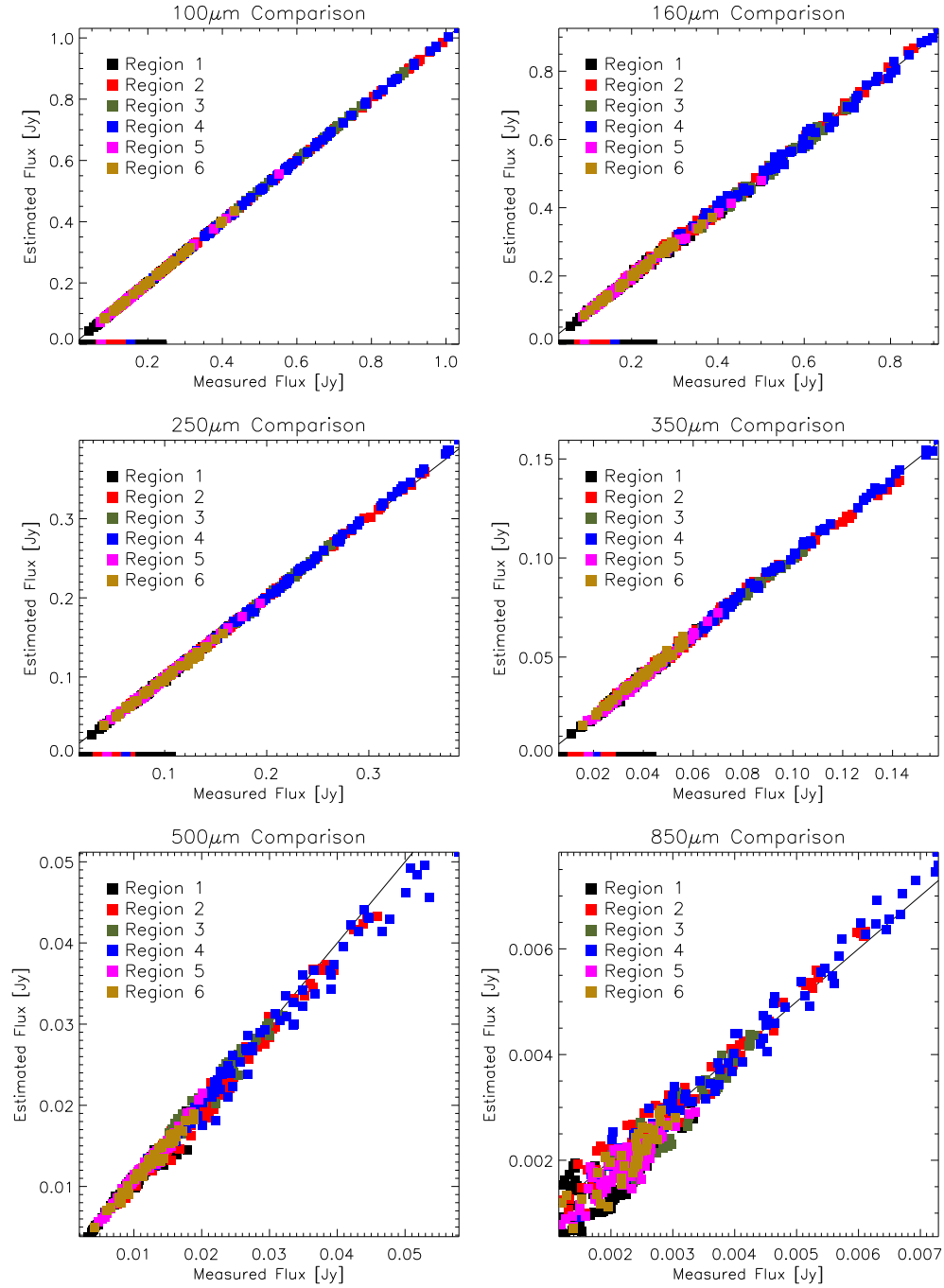
Figure 3.8: Quality of the SED fits with the emissivity index as a free paramter with the 500μm emission. The regions shown are the regions in figure 3.1.

Table 3.5.   Total Distance to 1 to 1 Line

Observation	Planck Model	Li and Draine Model	Variable Emissivity Index
100μm	0.000	0.01245	01277
160μm	15.55	8.979	2.159
250μm	5.808	3.072	0.4465
350μm	0.8045	0.3541	0.1161
500μm	0.02825	0.05218	0.09528
Total	23.01	12.58	3.131

3.2.2 Total Region Flux SED Fits

The second method used to determine the dust mass, was to fit the SED to the flux of each region in figure 3.1. Performing the fit in this manner is beneficial because it increases the signal to noise of the region and produces a more precise set of parameters. Initially, this style of fit was carried in the same fashion as the individual pixel fits by fixing the emissivity index to 1.8 and 2.0, and allowing the emissivity index to vary. However, given the greater range of mass values for the region fits, a single valued initial condition for the mass would produce a set of parameters that did not converge to the absolute minimum. The dependence of the initial mass and the converged parameter with a variable emissivity index are shown in figure 3.9. Similarly, if we fix the emissivity index, the dependence on the initial mass is nonexistent until the Levinberg-Marquardt method is unable to converge to an appropriate fit, figure 3.10.

Since we can't let emissivity index vary freely, an alternative method to determine it's value needs to be implemented. The emissivity index was de-

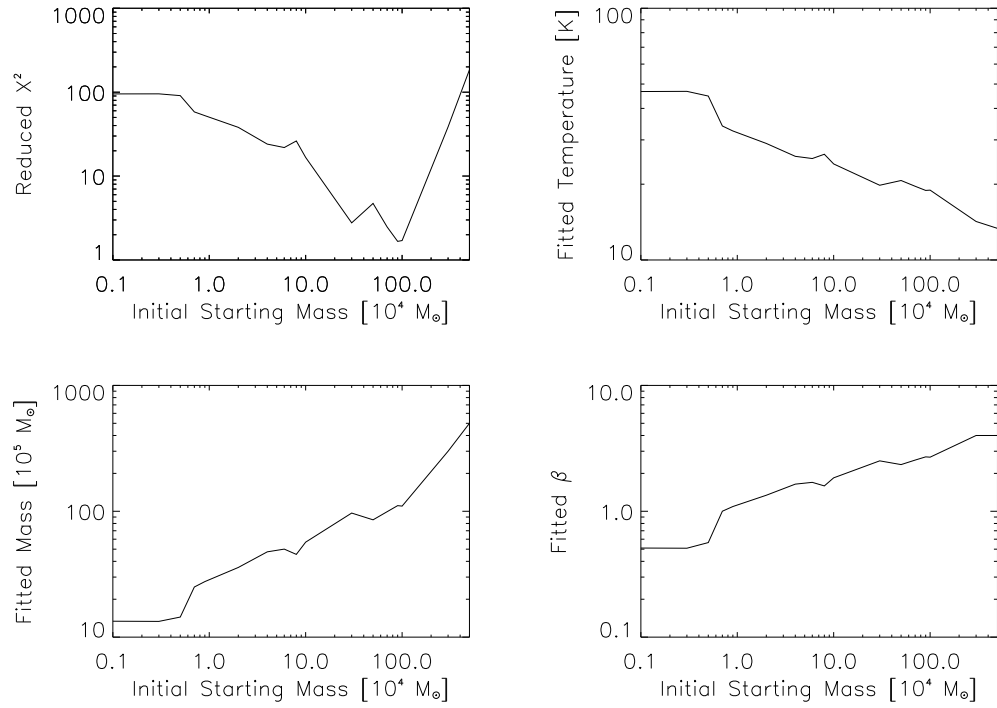Figure 3.9: Returned SED fitting output with Planck opacity for the χ^2, temperature, mass, and emissivity index with varying initial conditions. The top left panels shows the χ^2 values for each starting mass. The top right, bottom left, and bottom right panels show the returned temperatures, mass, and emissivity index.
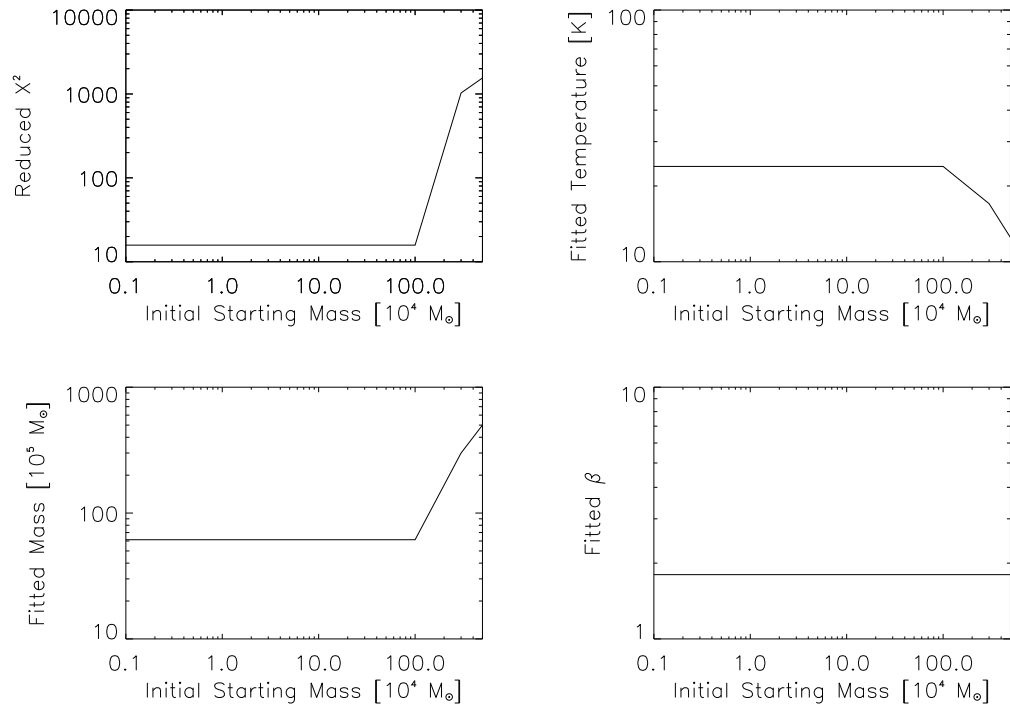
Figure 3.10: The same as figure 3.9, however the emissivity index has been fixed to 1.8.
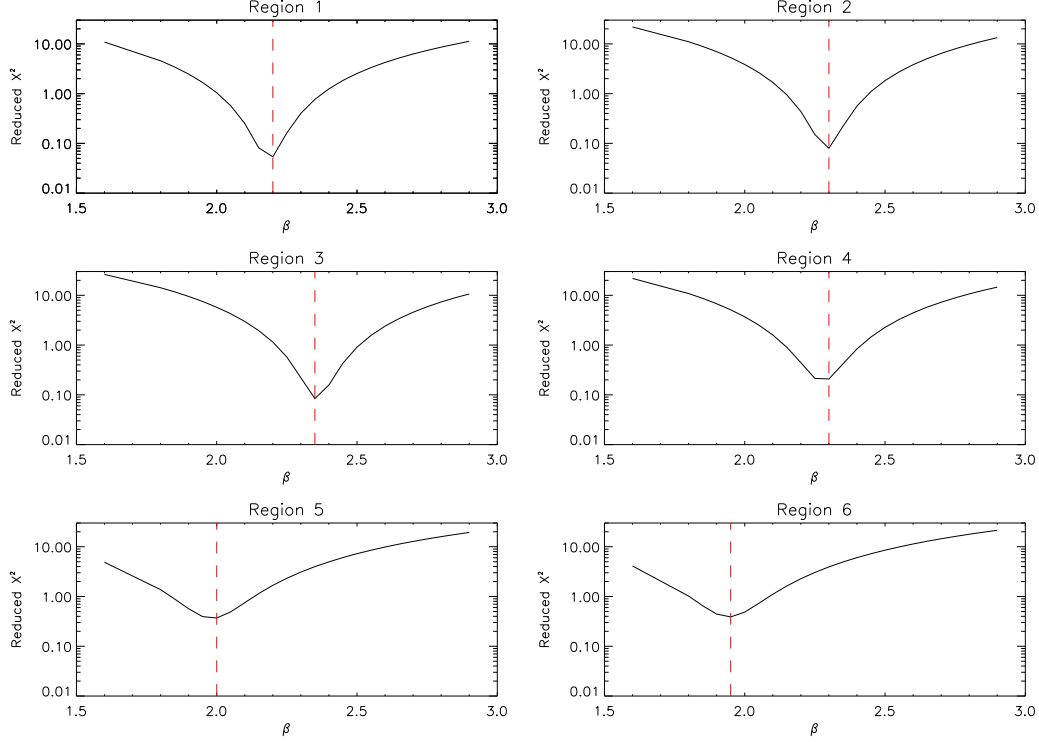
Figure 3.11: Plots for each region from figure 3.1 showing the fixed emissivity index value and the resulting reduced χ^2 value.

termined by fixing it over a range of 1.6 to 2.9 with a spacing of 0.05. The best emissivity index is determined by which value returns the lowest reduced χ^2. Plots showing the behavior of the χ^2 values with each emissivity index value are shown in figure 3.11 where the best value selected is represented by the red line. The results of each region using the fixed emissivity indices are shown in table 3.6, and their resulting SED's are shown in figure 3.12.
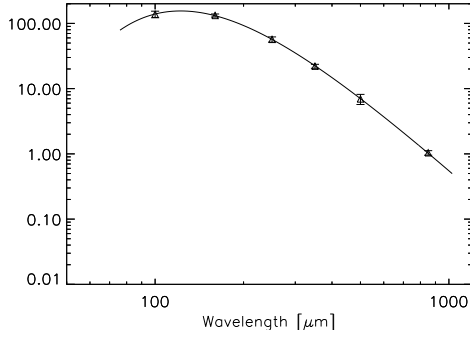
(a) Region 1 SED
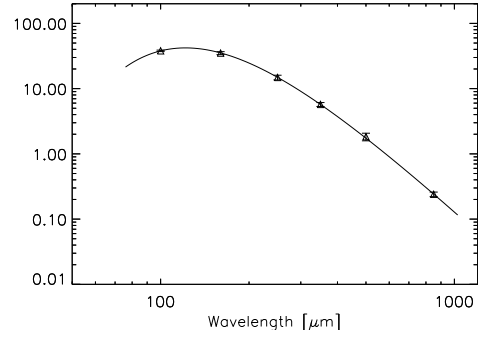
(b) Region 2 SED
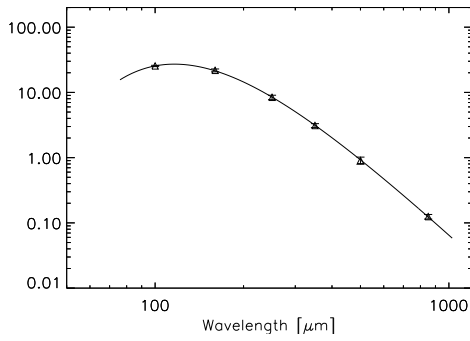
(c) Region 3 SED

(d) Region 4 SED
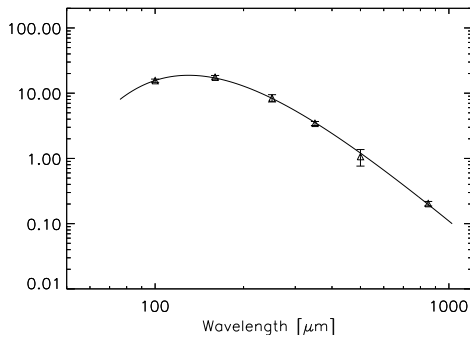
(e) Region 5 SED
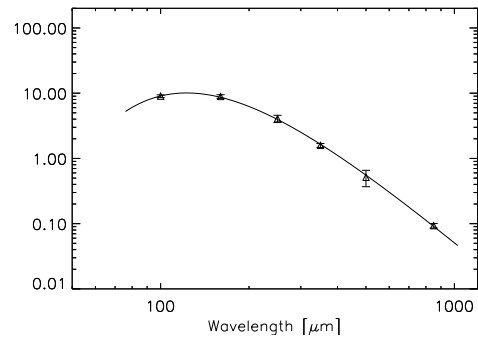
(f) Region 6 SED

Figure 3.12: SED fits for the flux of each region in figure 3.1 using the Planck Opacity.

Table 3.6.   Best Fit Parameters for Planck Opacity

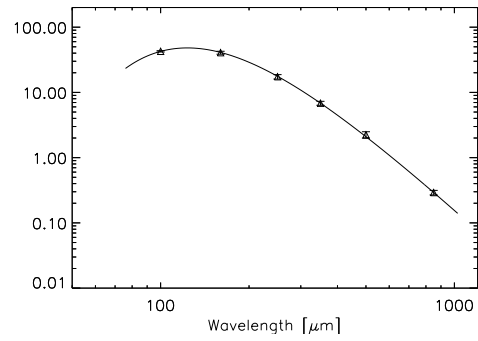| Region	Average β	Total Mass $[10^5 M_\odot]$	Surface Density $[M_\odot pc^{-2}]$	Average Temperature [K]
1	2.20 ± 0.03	70 ± 6	0.14 ± 0.01	22.8 ± 0.5
2	2.30 ± 0.03	19 ± 1	0.18 ± 0.01	22.5 ± 0.3
3	2.35 ± 0.03	9.6 ± 0.6	0.18 ± 0.01	23.3 ± 0.3
4	2.30 ± 0.03	23 ± 1	0.22 ± 0.01	22.2 ± 0.2
5	2.00 ± 0.03	11.3 ± 0.8	0.092 ± 0.007	22.3 ± 0.4
6	1.95 ± 0.03	4.5 ± 0.3	0.084 ± 0.006	23.9 ± 0.4

3.3 Discussion

3.3.1 Reliability of Individual Pixel Fits

The issue on whether or not the individual pixel fits are reliable is raised after seeing a strong dependence with the initial mass of the region SED fits shown in figure 3.9. Since any dependence on the initial mass has been removed in the global region fits, an agreement between the total pixel mass and the region fits would suggest that the initial mass used in the pixel fitting is an appropriate value. This is further strengthened by the smaller mass range of pixel fits. The smaller range allows the fitting method to hone into a smaller area of the χ^2 space avoiding any possible local minima to converge on.

3.3.2 Comparison with Previous Work

We can check the validity of our results by comparing them to previous SED fits using the KINGFISH data (Galametz et al., 2012). The best fit parameters from their fitting was T=20.2K±4K and β=2.3±0.2 which agree within error to our results of T=22K±1K and β=2.2±0.2 for a variable emissivity index. To test agreement with our mass we need to take into account several factors. The first being a lessened flux from the extended structure removal, and the second is the selection of the opacity value. Their reported mass for a variable emissivity index reported by Galametz et al. (2012) was $782^{+80}_{-66} \times 10^5 M_\odot$ for the sum of pixels in the parameter maps. We can scale the mass values by finding the ratio $\kappa_{Galametz}$ over κ_{Ours} which comes out to be 0.342. If we then scale by the amount of flux removed in the extended structure removal, we can scale the mass to $175^{+19}_{-17} \times 10^5 M_\odot$ which is above our maximum value of $108 \times 10^5 M_\odot$. This discrepancy can likely be attributed to how the total mass was found in each method. For our method we use the mass returned from fitting, and in Galametz et al. (2012) they use equation 3.4 using the 500μm emission to determine a dust mass.

3.3.3 Effects of 850μm Emission

The major difference between our work on NGC3627 and the work done in Galametz et al. (2012) is the presence of the 850μm data point. In our analysis the presence of the 850μm has shown little effect on the returned parameters. The returned values for a variable emissivity index are shown in table 3.7.

Table 3.7.   Best Fit Parameters Excluding 850μm Emission

Region	Average β	Total Mass $[10^5 M_\odot]$	Surface Density $[M_\odot pc^{-2}]$	Average Temperature [K]
1	2.3 ± 0.3	75 ± 29	0.15 ± 0.06	22 ± 2
2	2.3 ± 0.3	18 ± 5	0.17 ± 0.05	23 ± 2
3	2.4 ± 0.2	10 ± 1	0.19 ± 0.02	23 ± 1
4	2.2 ± 0.2	22 ± 5	0.21 ± 0.05	23 ± 2
5	2.3 ± 0.2	13 ± 3	0.11 ± 0.03	21 ± 1
6	2.2 ± 0.2	5 ± 1	0.10 ± 0.02	22 ± 1

The absence of a significant change in the returned parameters is indicative of a lack of any excess submillimeter emission suggestive of an abundance of a very cold (T $\lesssim$ 10K) dust component (Dale et al., 2012). This excess in emission is typically seen in low-metalicity systems such as dwarf galaxies (Madden et al., 2011), but has also been seen in NGC3627 (Galametz et al., 2014). While our results show no excess of emission at 850μm (evident in figures 3.6, 3.7, and 3.8), we should not expect to see any submillimeter excess given the $\log(O/H) + 12$ is either 8.34 or 8.99 depending on the calibration values used (Moustakas et al., 2010).

Bibliography

Abel, T., Anninos, P., Zhang, Y., & Norman, M. L. 1997, New A, 2, 181

Barrett, A. H. 1964, Nature, 202, 475

Bolatto, A. D., Wolfire, M., & Leroy, A. K. 2013, ARA&A, 51, 207

Burden, R. L. & Faires, J. D. 2001, Numerical analysis

Chapin, E. L., Berry, D. S., Gibb, A. G., Jenness, T., Scott, D., Tilanus, R. P. J., Economou, F., & Holland, W. S. 2013, MNRAS, 430, 2545

Dale, D. A., Aniano, G., Engelbracht, C. W., Hinz, J. L., Krause, O., Montiel, E. J., Roussel, H., Appleton, P. N., Armus, L., Beirão, P., Bolatto, A. D., Brandl, B. R., Calzetti, D., Crocker, A. F., Croxall, K. V., Draine, B. T., Galametz, M., Gordon, K. D., Groves, B. A., Hao, C.-N., Helou, G., Hunt, L. K., Johnson, B. D., Kennicutt, R. C., Koda, J., Leroy, A. K., Li, Y., Meidt, S. E., Miller, A. E., Murphy, E. J., Rahman, N., Rix, H.-W., Sandstrom, K. M., Sauvage, M., Schinnerer, E., Skibba, R. A., Smith, J.-D. T., Tabatabaei, F. S., Walter, F., Wilson, C. D., Wolfire, M. G., & Zibetti, S. 2012, ApJ, 745, 95

Dempsey, J. T., Friberg, P., Jenness, T., Tilanus, R. P. J., Thomas, H. S., Holland, W. S., Bintley, D., Berry, D. S., Chapin, E. L., Chrysostomou, A., Davis, G. R., Gibb, A. G., Parsons, H., & Robson, E. I. 2013, MNRAS, 430, 2534

Dobbs, C. L., Krumholz, M. R., Ballesteros-Paredes, J., Bolatto, A. D., Fukui, Y., Heyer, M., Mac Low, M.-M., Ostriker, E. C., & Vázquez-Semadeni, E. 2013, ArXiv e-prints

Drabek, E., Hatchell, J., Friberg, P., Richer, J., Graves, S., Buckle, J. V., Nutter, D., Johnstone, D., & Di Francesco, J. 2012, MNRAS, 426, 23

Draine, B. T. 2011, Physics of the Interstellar and Intergalactic Medium

Elmegreen, B. G. 1987, ApJ, 312, 626

Field, G. B. & Saslaw, W. C. 1965, ApJ, 142, 568

Galametz, M., Albrecht, M., Kennicutt, R., Aniano, G., Bertoldi, F., Calzetti, D., Croxall, K. V., Dale, D., Draine, B., Engelbracht, C., Gordon, K., Hinz, J., Hunt, L. K., Kirkpatrick, A., Murphy, E., Roussel, H., Skibba, R. A., Walter, F., Weiss, A., & Wilson, C. D. 2014, MNRAS, 439, 2542

Galametz, M., Kennicutt, R. C., Albrecht, M., Aniano, G., Armus, L., Bertoldi, F., Calzetti, D., Crocker, A. F., Croxall, K. V., Dale, D. A., Donovan Meyer, J., Draine, B. T., Engelbracht, C. W., Hinz, J. L., Roussel, H., Skibba, R. A., Tabatabaei, F. S., Walter, F., Weiss, A., Wilson, C. D., & Wolfire, M. G. 2012, MNRAS, 425, 763

Gavin, H. P. 2013, The Levenberg-Marquardt method for nonlinear least squares curve-fitting problems, Tech. rep., Department of Civil and Environmental Engineering, Duke University

Glover, S. C. O. 2003, ApJ, 584, 331

66

Gould, R. J. & Salpeter, E. E. 1963, ApJ, 138, 393

Gry, C., Boulanger, F., Nehmé, C., Pineau des Forêts, G., Habart, E., & Falgarone, E. 2002, A&A, 391, 675

Herbst, E., Chang, Q., & Cuppen, H. M. 2005, Journal of Physics Conference Series, 6, 18

Holland, W. S., Bintley, D., Chapin, E. L., Chrysostomou, A., Davis, G. R., Dempsey, J. T., Duncan, W. D., Fich, M., Friberg, P., Halpern, M., Irwin, K. D., Jenness, T., Kelly, B. D., MacIntosh, M. J., Robson, E. I., Scott, D., Ade, P. A. R., Atad-Ettedgui, E., Berry, D. S., Craig, S. C., Gao, X., Gibb, A. G., Hilton, G. C., Hollister, M. I., Kycia, J. B., Lunney, D. W., McGregor, H., Montgomery, D., Parkes, W., Tilanus, R. P. J., Ullom, J. N., Walther, C. A., Walton, A. J., Woodcraft, A. L., Amiri, M., Atkinson, D., Burger, B., Chuter, T., Coulson, I. M., Doriese, W. B., Dunare, C., Economou, F., Niemack, M. D., Parsons, H. A. L., Reintsema, C. D., Sibthorpe, B., Smail, I., Sudiwala, R., & Thomas, H. S. 2013, MNRAS, 430, 2513

Jura, M. 1975, ApJ, 197, 575

Kennicutt, R. C., Calzetti, D., Aniano, G., Appleton, P., Armus, L., Beirão, P., Bolatto, A. D., Brandl, B., Crocker, A., Croxall, K., Dale, D. A., Meyer, J. D., Draine, B. T., Engelbracht, C. W., Galametz, M., Gordon, K. D., Groves, B., Hao, C.-N., Helou, G., Hinz, J., Hunt, L. K., Johnson, B., Koda, J., Krause, O., Leroy, A. K., Li, Y., Meidt, S., Montiel, E., Murphy, E. J., Rahman, N., Rix, H.-W., Roussel, H., Sandstrom, K., Sauvage, M.,

Schinnerer, E., Skibba, R., Smith, J. D. T., Srinivasan, S., Vigroux, L., Walter, F., Wilson, C. D., Wolfire, M., & Zibetti, S. 2011, PASP, 123, 1347

Kennicutt, R. C. & Evans, N. J. 2012, ARA&A, 50, 531

Kennicutt, Jr., R. C., Armus, L., Bendo, G., Calzetti, D., Dale, D. A., Draine, B. T., Engelbracht, C. W., Gordon, K. D., Grauer, A. D., Helou, G., Hollenbach, D. J., Jarrett, T. H., Kewley, L. J., Leitherer, C., Li, A., Malhotra, S., Regan, M. W., Rieke, G. H., Rieke, M. J., Roussel, H., Smith, J.-D. T., Thornley, M. D., & Walter, F. 2003, PASP, 115, 928

Kim, W.-T. & Ostriker, E. C. 2001, ApJ, 559, 70

Krumholz, M. R. 2014, ArXiv e-prints

Kuno, N., Sato, N., Nakanishi, H., Hirota, A., Tosaki, T., Shioya, Y., Sorai, K., Nakai, N., Nishiyama, K., & Vila-Vilaró, B. 2007, PASJ, 59, 117

Kwan, J. 1979, ApJ, 229, 567

Leroy, A. K., Walter, F., Bigiel, F., Usero, A., Weiss, A., Brinks, E., de Blok, W. J. G., Kennicutt, R. C., Schuster, K.-F., Kramer, C., Wiesemeyer, H. W., & Roussel, H. 2009, AJ, 137, 4670

Li, A. & Draine, B. T. 2001, ApJ, 554, 778

Madden, S. C., Galametz, M., Cormier, D., Lebouteiller, V., Galliano, F., Hony, S., Rémy, A., Sauvage, M., Contursi, A., Sturm, E., Poglitsch, A., Pohlen, M., Smith, M. W. L., Bendo, G., & O'Halloran, B. 2011, in EAS Publications Series, Vol. 52, EAS Publications Series, ed. M. Röllig, R. Simon, V. Ossenkopf, & J. Stutzki, 95–101

Markwardt, C. B. 2009, in Astronomical Society of the Pacific Conference Series, Vol. 411, Astronomical Data Analysis Software and Systems XVIII, ed. D. A. Bohlender, D. Durand, & P. Dowler, 251

McKee, C. F. & Ostriker, E. C. 2007, ARA&A, 45, 565

Moustakas, J., Kennicutt, Jr., R. C., Tremonti, C. A., Dale, D. A., Smith, J.-D. T., & Calzetti, D. 2010, ApJS, 190, 233

Palla, F., Salpeter, E. E., & Stahler, S. W. 1983, ApJ, 271, 632

Parker, E. N. 1966, ApJ, 145, 811

Pirronello, V., Liu, C., Shen, L., & Vidali, G. 1997, ApJ, 475, L69

Planck Collaboration, Abergel, A., Ade, P. A. R., Aghanim, N., Arnaud, M., Ashdown, M., Aumont, J., Baccigalupi, C., Balbi, A., Banday, A. J., Barreiro, R. B., Bartlett, J. G., Battaner, E., Benabed, K., Benoît, A., Bernard, J.-P., Bersanelli, M., Bhatia, R., Bock, J. J., Bonaldi, A., Bond, J. R., Borrill, J., Bouchet, F. R., Boulanger, F., Bucher, M., Burigana, C., Cabella, P., Cardoso, J.-F., Catalano, A., Cayón, L., Challinor, A., Chamballu, A., Chiang, L.-Y., Chiang, C., Christensen, P. R., Clements, D. L., Colombi, S., Couchot, F., Coulais, A., Crill, B. P., Cuttaia, F., Danese, L., Davies, R. D., Davis, R. J., de Bernardis, P., de Gasperis, G., de Rosa, A., de Zotti, G., Delabrouille, J., Delouis, J.-M., Désert, F.-X., Dickinson, C., Dobashi, K., Donzelli, S., Doré, O., Dörl, U., Douspis, M., Dupac, X., Efstathiou, G., Enßlin, T. A., Eriksen, H. K., Finelli, F., Forni, O., Frailis, M., Franceschi, E., Galeotta, S., Ganga, K., Giard, M., Giardino, G., Giraud-Héraud, Y., González-Nuevo, J., Górski, K. M., Gratton, S., Gregorio, A., Gruppuso,

A., Guillet, V., Hansen, F. K., Harrison, D., Henrot-Versillé, S., Herranz, D., Hildebrandt, S. R., Hivon, E., Hobson, M., Holmes, W. A., Hovest, W., Hoyland, R. J., Huffenberger, K. M., Jaffe, A. H., Jones, A., Jones, W. C., Juvela, M., Keihänen, E., Keskitalo, R., Kisner, T. S., Kneissl, R., Knox, L., Kurki-Suonio, H., Lagache, G., Lamarre, J.-M., Lasenby, A., Laureijs, R. J., Lawrence, C. R., Leach, S., Leonardi, R., Leroy, C., Linden-Vørnle, M., López-Caniego, M., Lubin, P. M., Macías-Pérez, J. F., MacTavish, C. J., Maffei, B., Mandolesi, N., Mann, R., Maris, M., Marshall, D. J., Martin, P., Martínez-González, E., Masi, S., Matarrese, S., Matthai, F., Mazzotta, P., McGehee, P., Meinhold, P. R., Melchiorri, A., Mendes, L., Mennella, A., Mitra, S., Miville-Deschênes, M.-A., Moneti, A., Montier, L., Morgante, G., Mortlock, D., Munshi, D., Murphy, A., Naselsky, P., Natoli, P., Netterfield, C. B., Nørgaard-Nielsen, H. U., Noviello, F., Novikov, D., Novikov, I., Osborne, S., Pajot, F., Paladini, R., Pasian, F., Patanchon, G., Perdereau, O., Perotto, L., Perrotta, F., Piacentini, F., Piat, M., Plaszczynski, S., Pointecouteau, E., Polenta, G., Ponthieu, N., Poutanen, T., Prézeau, G., Prunet, S., Puget, J.-L., Reach, W. T., Rebolo, R., Reinecke, M., Renault, C., Ricciardi, S., Riller, T., Ristorcelli, I., Rocha, G., Rosset, C., Rubiño-Martín, J. A., Rusholme, B., Sandri, M., Santos, D., Savini, G., Scott, D., Seiffert, M. D., Shellard, P., Smoot, G. F., Starck, J.-L., Stivoli, F., Stolyarov, V., Sudiwala, R., Sygnet, J.-F., Tauber, J. A., Terenzi, L., Toffolatti, L., Tomasi, M., Torre, J.-P., Tristram, M., Tuovinen, J., Umana, G., Valenziano, L., Verstraete, L., Vielva, P., Villa, F., Vittorio, N., Wade, L. A., Wandelt, B. D., Yvon, D., Zacchei, A., & Zonca, A. 2011, A&A, 536, A25

Reuter, H.-P., Sievers, A. W., Pohl, M., Lesch, H., & Wielebinski, R. 1996, A&A, 306, 721

Sandstrom, K. M., Leroy, A. K., Walter, F., Bolatto, A. D., Croxall, K. V., Draine, B. T., Wilson, C. D., Wolfire, M., Calzetti, D., Kennicutt, R. C., Aniano, G., Donovan Meyer, J., Usero, A., Bigiel, F., Brinks, E., de Blok, W. J. G., Crocker, A., Dale, D., Engelbracht, C. W., Galametz, M., Groves, B., Hunt, L. K., Koda, J., Kreckel, K., Linz, H., Meidt, S., Pellegrini, E., Rix, H.-W., Roussel, H., Schinnerer, E., Schruba, A., Schuster, K.-F., Skibba, R., van der Laan, T., Appleton, P., Armus, L., Brandl, B., Gordon, K., Hinz, J., Krause, O., Montiel, E., Sauvage, M., Schmiedeke, A., Smith, J. D. T., & Vigroux, L. 2013, ApJ, 777, 5

Walter, F., Brinks, E., de Blok, W. J. G., Bigiel, F., Kennicutt, Jr., R. C., Thornley, M. D., & Leroy, A. 2008, AJ, 136, 2563

Wilson, C. D., Warren, B. E., Israel, F. P., Serjeant, S., Attewell, D., Bendo, G. J., Butner, H. M., Chanial, P., Clements, D. L., Golding, J., Heesen, V., Irwin, J., Leech, J., Matthews, H. E., Mühle, S., Mortier, A. M. J., Petitpas, G., Sánchez-Gallego, J. R., Sinukoff, E., Shorten, K., Tan, B. K., Tilanus, R. P. J., Usero, A., Vaccari, M., Wiegert, T., Zhu, M., Alexander, D. M., Alexander, P., Azimlu, M., Barmby, P., Brar, R., Bridge, C., Brinks, E., Brooks, S., Coppin, K., Côté, S., Côté, P., Courteau, S., Davies, J., Eales, S., Fich, M., Hudson, M., Hughes, D. H., Ivison, R. J., Knapen, J. H., Page, M., Parkin, T. J., Rigopoulou, D., Rosolowsky, E., Seaquist, E. R., Spekkens, K., Tanvir, N., van der Hulst, J. M., van der Werf, P., Vlahakis, C., Webb, T. M., Weferling, B., & White, G. J. 2012, MNRAS, 424, 3050

Wolfire, M. G., McKee, C. F., Hollenbach, D., & Tielens, A. G. G. M. 2003, ApJ, 587, 278

Wolfire, M. G., Tielens, A. G. G. M., Hollenbach, D., & Kaufman, M. J. 2008, ApJ, 680, 384